Image reconstruction from structured subsampled 2D DFT data

Gerlind Plonka* and Anahita Riahi*

June 4, 2025

Abstract

In this paper we study the performance of image reconstruction methods from incomplete samples of the 2D discrete Fourier transform. Inspired by requirements in parallel MRI, we focus on a special sampling pattern with a small number of acquired rows of the Fourier transformed image $\hat{\mathbf{A}}$. We show the importance of the low-pass set of acquired rows around zero in the Fourier space for image reconstruction. A suitable choice of the width L of this index set depends on the image data and is crucial to achieve optimal reconstruction results. We show that linear reconstruction approaches cannot lead to satisfying recovery results. We propose a new hybrid algorithm which connects the TV minimization technique based on primal-dual optimization with a recovery algorithm which exploits properties of the special sampling pattern for reconstruction. Our method shows very good performance for natural images as well as for cartoon-like images for a data reduction rate up to 8 in the complex setting and even 16 for real images.

Key words. discrete Fourier transform, interpolation methods, total variation minimization, primal-dual algorithm, local total variation, incomplete Fourier data
AMS Subject classifications. 65T50, 42A38, 42B05, 49M27, 68U10

1 Introduction

In this paper we study the problem of how to efficiently reconstruct a two-dimensional image $\mathbf{A} \in \mathbb{C}^{N \times M}$ from structured undersampled 2D DFT data.

Incomplete Fourier data arise in different application fields, as for example in magnetic resonance imaging (MRI), see e.g. [2, 8, 10, 12, 14, 16, 19, 18, 24, 27, 28], seismic imaging [25], or computerized tomography [13, 23]. Depending on the applications, the patterns of incomplete Fourier measurements have different structures. Discrete subsampling is mostly performed on a two-dimensional cartesian grid or on a polar grid in frequency domain. Several recovery algorithms focus on the polar grid, see e.g. [2, 8, 15, 18, 27] or on (structured) random undersampling on the cartesian grid [1, 4, 17, 20, 26], where in both cases the Fourier sampling pattern is denser for low frequencies.

*University of Göttingen, Institute for Numerical and Applied Mathematics, Lotzestr. 16-18, 37083 Göttingen, Germany. Email: (plonka,a.riahi)@math.uni-goettingen.de, Corresponding Author: Gerlind Plonka (Orcid: https://orcid.org/0000-0002-3232-0573)

However, in most applications, a random undersampling is not possible or technically too expensive. For example, in MRI only samples along a line or a smooth curve can be efficiently acquired, and every new line takes additional acquisition time. Moreover, in parallel MRI, one acquires simultaneously subsampled Fourier measurements along lines corresponding to different coils, and the challenge is to reconstruct the complete magnetization image from the incomplete Fourier samples of these coil images, see e.g. [2, 10, 11, 19, 22, 24].

Recovery methods in MRI based on interpolation or approximation of non-aquired data in the Fourier domain as [10, 19], or on subspace methods [24], are particularly based on special sampling patterns consisting of a bounded number of horizontal (or vertical) lines.

In the discrete setting, we assume that an image $\mathbf{A}$ has to be recovered from a subsampled set of components of its discrete Fourier transform $\hat{\mathbf{A}} = \mathbf{F}_N \mathbf{A} \mathbf{F}_M$. This reconstruction problem is ill-posed, since the Fourier basis is orthonormal, and the reconstruction is therefore not unique. In order to still achieve suitable reconstruction results, certain a priori assumptions on the image to be recovered are essential.

Considering the image in a vectorized form $\mathrm{vec}(\mathbf{A})$, the reconstruction problem can also be rewritten as the problem to find a solution vector of an incomplete linear system, where only a subset of the equations of the system $(\mathbf{F}_N \otimes \mathbf{F}_M)\mathrm{vec}(\mathbf{A}) = \mathrm{vec}(\hat{\mathbf{A}})$ is available. Here, one cannot assume that $\mathrm{vec}(\mathbf{A})$ is a sparse vector or has a particularly small 1-norm. Instead, one natural a priori assumption on the image $\mathbf{A}$ is that it is piecewise smooth. In most reconstruction methods, this is transferred to a constraint that $\mathbf{A}$ has a small total variation and/or a sparse representation in some wavelet frame. These constraints can be incorporated into a minimization problem to cope for the missing Fourier data. Since the total variation constraint often produces staircasing artifacts, many papers either focus on numerical examples with piecewise constant images (as "phantom" images) or try to extend or to generalize the constraints on the image, for example by using generalized TV [15], special filters [1, 26], or sparsity in wavelet frames [27].

Inspired by the special requirements for MRI reconstructions, we study in this paper the reconstruction from subsampled 2D DFT measurements for the special sampling grid which consists of a fixed number of horizontal lines, i.e., we assume that only a certain number of rows of $\hat{\mathbf{A}}$ is available to recover $\mathbf{A}$. We will investigate, how these rows should be taken, in order to achieve very good recovery results based on a suitable reconstruction method. In particular, we will examine, how the special structure of the considered sampling pattern influences the reconstruction, and how the pattern can be exploited to improve the image recovery. We will survey some currently used methods for image reconstruction based on our sampling pattern and propose a new hybrid method, which outperforms other approaches for natural images as well as cartoon-like images.

Problem description. For a given discrete image $\mathbf{A} = (a_{j_1,j_2})_{j_1=-n,j_2=-m}^{n-1,m-1} \in \mathbb{C}^{N\times M}$ with N, M being even positive integers with $N = 2n$ and $M = 2m$, the discrete two-dimensional Fourier transform is given by

$$\hat{\mathbf{A}} = \mathbf{F}_N \, \mathbf{A} \, \mathbf{F}_M,$$

where $\mathbf{F}_N = \frac{1}{\sqrt{N}}(\omega_N^{jk})_{j,k=-n}^{n-1}$ and $\mathbf{F}_M = \frac{1}{\sqrt{M}}(\omega_M^{jk})_{j,k=-m}^{m-1}$ denote the centered unitary Fourier matrices, and $\omega_N := \mathrm{e}^{-2\pi\mathrm{i}/N}$. The components $\hat{a}_{\nu_1,\nu_2}$ of $\hat{\mathbf{A}}$ have the form

$$\hat{a}_{\nu_1,\nu_2} = \frac{1}{\sqrt{MN}} \sum_{k_1=-n}^{n-1} \sum_{k_2=-m}^{m-1} a_{k_1,k_2} \, \omega_N^{k_1\nu_1} \omega_M^{k_2\nu_2}.$$

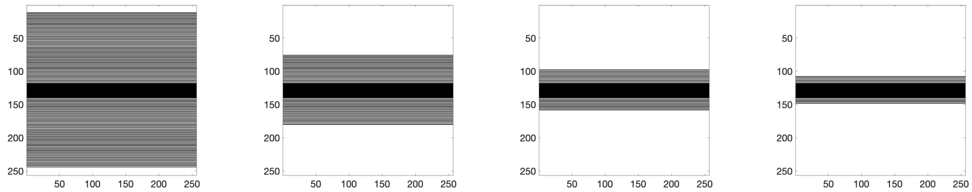

Figure 1: Masks for acquired Fourier data for an 256×256 image with width $L = 21$ of the low-pass set and reduction rates $r = 2, 4, 6, 8$, where black lines illustrate the acquired rows

The inverse two-dimensional discrete Fourier transform is given by $\mathbf{A} = \overline{\mathbf{F}}_N \, \hat{\mathbf{A}} \, \overline{\mathbf{F}}_M$, since we have $\mathbf{F}_N^{-1} = \overline{\mathbf{F}}_N$. Throughout the paper, we assume for simplicity that N is a multiple of 8, such that $\frac{n}{2} = \frac{N}{4}$ and $\frac{n}{4} = \frac{N}{8}$ are integers.

Let $\Lambda_{N,M} := \{-n, \ldots, n-1\} \times \{-m, \ldots, m-1\}$ denote the index set corresponding to the $(N \times M)$-image. We use the 2D index notation $\boldsymbol{\nu} = (\nu_1, \nu_2) \in \Lambda_{N,M}$.

We will study the problem of how to reconstruct the image $\mathbf{A}$ from incomplete 2D DFT data $\hat{a}_{\boldsymbol{\nu}}$, $\boldsymbol{\nu} \in \Lambda \subset \Lambda_{N,M}$, where the subset Λ corresponding to the acquired DFT data has the special form

$$\Lambda := \Lambda_{L,M} \cup \Lambda_{N/r,M}. \tag{1.1}$$

The two index sets $\Lambda_{L,M}$ and $\Lambda_{N/r,M}$ will be fixed in the sequel. Here, r denotes the *reduction rate*, i.e., $\lfloor \frac{N}{r} \rfloor$ (or $\lfloor \frac{N}{r} \rfloor - 1$, if $\lfloor \frac{N}{r} \rfloor$ is even) is the number of acquired rows of $\hat{\mathbf{A}}$ and $|\Lambda| = M \lfloor \frac{N}{r} \rfloor$ the number of all acquired DFT data.
We assume that $L = 2\ell + 1$ with odd ℓ, then

$$\Lambda_{L,M} := \Lambda_L \times \Lambda_M \quad \text{with} \quad \Lambda_L := \{-\ell, \ldots, \ell\}, \quad \Lambda_M := \{-m, \ldots, m-1\},$$

denotes the *low-pass set*, where $\ell < \frac{n}{r} = \frac{N}{2r}$. In parallel MRI this set is called *calibration set*. In other words, we assume that the centered rows of $\hat{\mathbf{A}}$ with indices $-\ell, -\ell+1, \ldots, \ell-1, \ell$ are completely acquired. Outside this low-pass set, only a certain amount of further rows of $\hat{\mathbf{A}}$ is acquired. We will particularly focus on the sampling pattern, where further data are required along every second row (symmetrically with respect to the image center) until the bound of $\lfloor \frac{N}{r} \rfloor$ is reached, since this pattern usually provides the best reconstruction results. Therefore, the second index set is determined as a symmetric subset of odd-indexed rows

$$\Lambda_{N/r,M} := \{-2\kappa+1, -2\kappa+3, \ldots, 2\kappa-3, 2\kappa-1\} \times \Lambda_M, \tag{1.2}$$

such that $\{-2\kappa+1, -2\kappa+3, \ldots, 2\kappa-3, 2\kappa-1\} \cup \{-\ell, \ldots, \ell\}$ contains $\lfloor \frac{N}{r} \rfloor$ (or $\lfloor \frac{N}{r} \rfloor - 1$) elements. More precisely, $\kappa := \frac{\ell+1}{2} + \lfloor \frac{N}{2r} - \frac{L}{2} \rfloor$, such that beside the low-pass area, also the $\lfloor \frac{N}{2r} - \frac{L}{2} \rfloor$ rows with indices $\ell+2, \ell+4, \ldots, 2\kappa-1$ and the $\lfloor \frac{N}{2r} - \frac{L}{2} \rfloor$ rows with indices $-\ell-2, -\ell-4, \ldots, -2\kappa+1$ are acquired. Figure 1 displays the masks of acquired data for $N = M = 256$, $L = 21$ and reduction rates $2, 4, 6, 8$, where beside the 21 fully acquired rows at the center every second further row is taken such together we have 127 rows for $r = 2$, 63 rows for $r = 4$ etc..
We denote with $\mathbf{P}^{(\Lambda)} = (p_{\boldsymbol{\nu}}^{(\Lambda)})_{\boldsymbol{\nu} \in \Lambda_{N,M}}$ the projection matrix (mask) corresponding to the sampling set Λ in (1.1), i.e., $p_{\boldsymbol{\nu}} = 1$ if $\boldsymbol{\nu} \in \Lambda$ and $p_{\boldsymbol{\nu}} = 0$ otherwise. Thus, $\mathbf{P}^{(\Lambda)}$ contains rows of ones and zero rows. Then we can formulate the reconstruction problem as follows: Find an optimal reconstruction $\tilde{\mathbf{A}}$ of $\mathbf{A}$ from the incomplete 2D DFT data, i.e., with

$$\mathbf{P}^{(\Lambda)} \circ \hat{\tilde{\mathbf{A}}} = \mathbf{P}^{(\Lambda)} \circ \hat{\mathbf{A}} = \mathbf{P}^{(\Lambda)} \circ (\mathbf{F}_N \mathbf{A} \mathbf{F}_M), \tag{1.3}$$

where $\circ$ denotes the pointwise product. The reconstruction quality will be measured in the Frobenius norm, i.e., for the reconstruction $\tilde{\mathbf{A}}$ we will consider the error $\|\tilde{\mathbf{A}} - \mathbf{A}\|_F = (\sum_{k_1=-n}^{n-1} \sum_{k_2=-m}^{m-1} |\tilde{a}_{k_1,k_2} - a_{k_1,k_2}|^2)^{1/2} = \sum_{\mathbf{k}\in\Lambda_{N,M}} |\tilde{a}_{\mathbf{k}} - a_{\mathbf{k}}|^2)^{1/2}$, or the peak signal to noise ratio PSNR$= 10\log_{10}\big(\frac{NM}{\|\tilde{\mathbf{A}}-\mathbf{A}\|_F^2}\big)$.

Observe that for complex images $\mathbf{A} = \mathbf{A}_R + \mathrm{i}\mathbf{A}_I = (a_{R,\mathbf{k}} + \mathrm{i}a_{I,\mathbf{k}})_{\mathbf{k}\in\Lambda_{N,M}}$ with $\mathbf{A}_R, \mathbf{A}_I \in \mathbb{R}^{N\times M}$, we can reconstruct $\mathbf{A}_R$ and $\mathbf{A}_I$ separately, since the sampling set is taken symmetrically, i.e., for acquired $\hat{a}_{\boldsymbol{\nu}} = \hat{a}_{\nu_1,\nu_2}$, we also have acquired $\hat{a}_{-\boldsymbol{\nu}} = \hat{a}_{-\nu_1,-\nu_2}$. Indeed, we have for all $\boldsymbol{\nu} \in \Lambda_{N,M}$

$$\tfrac{1}{2}(\hat{a}_{\boldsymbol{\nu}} + \overline{\hat{a}_{-\boldsymbol{\nu}}}) = \tfrac{1}{2}\Big(\sum_{\mathbf{k}\in\Lambda_{N,M}} (a_{R,\mathbf{k}} + \mathrm{i}a_{I,\mathbf{k}})\,\omega_N^{\boldsymbol{\nu}\cdot\mathbf{k}} + \sum_{\mathbf{k}\in\Lambda_{N,M}} \overline{(a_{R,\mathbf{k}} + \mathrm{i}a_{I,\mathbf{k}})}\,\omega_N^{\boldsymbol{\nu}\cdot\mathbf{k}}\Big) = \hat{a}_{R,\boldsymbol{\nu}},$$

$$\tfrac{1}{2}(\hat{a}_{\boldsymbol{\nu}} - \overline{\hat{a}_{-\boldsymbol{\nu}}}) = \tfrac{1}{2}\Big(\sum_{\mathbf{k}\in\Lambda_{N,M}} (a_{R,\mathbf{k}} - \mathrm{i}a_{I,\mathbf{k}})\,\omega_N^{\boldsymbol{\nu}\cdot\mathbf{k}} + \sum_{\mathbf{k}\in\Lambda_{N,M}} \overline{(a_{R,\mathbf{k}} - \mathrm{i}a_{I,\mathbf{k}})}\,\omega_N^{\boldsymbol{\nu}\cdot\mathbf{k}}\Big) = \hat{a}_{I,\boldsymbol{\nu}}.$$

In other words, to reconstruct a real image $\mathbf{A}$ we can reduce the index set of acquired data to

$$\Lambda = \Big(\{0, 1, \dots, \ell\} \cup \{1, 3, \dots, 2\kappa - 1\}\Big) \times \Lambda_M$$

such that a reduction rate r considered in this paper corresponds in the real case to a reduction rate of almost $2r$.

Outline of this paper. In Section 2, we will explain in detail, why this reconstruction problem is indeed challenging. We will show, why a suitable choice of the width L of the low-pass set is crucial to achieve a desired reconstruction quality. Further, we discuss the limitations of direct reconstruction approaches, such as zero refilling, linear interpolation, and adaptive interpolation, all of which fail to produce satisfactory reconstruction results.

In Section 3, we propose an iterative reconstruction algorithm based on total variation minimization of the resulting image. The arising functional is minimized using the primal dual algorithm [6]. Furthermore, in Section 4, we present a new hybrid algorithm, which connects the TV-minimization reconstruction with an adaptive reconstruction improvement by exploiting the data knowledge that can be extracted from the special sampling pattern.

In Section 5, we present several examples of image reconstruction and show the very good performance of our hybrid algorithm for data reduction rates of up to 8 (that is, 16 in the real case). In particular, our algorithm always essentially improves the reconstruction that can be obtained by taking just the corresponding amount of low-pass data. We also show numerically that other sampling schemes, where besides the low-pass area every third or every fourth row of $\hat{\mathbf{A}}$ is acquired until the upper bound of $\lfloor \frac{N}{r} \rfloor$ is reached, do not lead to better reconstruction results.

Further notations. For the sampling set in (1.1), we use the notation $\Lambda = \Lambda_1 \times \Lambda_M$, where Λ_1 contains the indices of all acquired rows, i.e.,

$$\Lambda_1 := \Lambda_L \cup \Lambda_\kappa = \{-\ell, \dots, \ell\} \cup \{-2\kappa + 1, -2\kappa + 3, \dots, 2\kappa - 3, 2\kappa - 1\}. \tag{1.4}$$

Further, $\mathrm{vec}(\mathbf{A})$ denotes the columnwise vectorization of a matrix $\mathbf{A}$, and $\mathbf{A} \otimes \mathbf{B}$ is the Kronecker product of $\mathbf{A} \in \mathbb{C}^{2n\times 2m}$, $\mathbf{B} \in \mathbb{C}^{N_2\times M_2}$ given by

$$\mathbf{A} \otimes \mathbf{B} = (a_{k_1,k_2}\mathbf{B})_{k_1=-n,k_2=-m}^{n-1,m-1} \in \mathbb{C}^{2nN_2\times 2mM_2}.$$

The identity matrix is always denoted by $\mathbf{I}$, and its dimension follows from the context.

2 Challenges of the reconstruction problem

In this section, we first summarize some facts about the reconstruction challenges from incomplete 2D-DFT data for the described sampling pattern. Then we will give a short overview of simple reconstruction ideas and show their weaknesses for the reconstruction problem at hand.

2.1 Importance of the low-pass set

As introduced in (1.1), we assume that acquired Fourier data are given with respect to the index set Λ, which consists of the low-pass set $\Lambda_{L,M}$ containing the rows of $\hat{\mathbf{A}}$ with indices $-\ell, \ldots, \ell$ and the set $\Lambda_{N/r,M}$ containing each second (odd-indexed) row of $\hat{\mathbf{A}}$ until the bound of $\lfloor N/r \rfloor$ acquired rows is reached. Assume for a moment that $L = 0$ and $r = 2$, such that the index set corresponding to acquired entries is given by $\Lambda_{N/r,M}$ in (1.2) with $\kappa = \frac{n}{2}$. In this case, every second row of $\hat{\mathbf{A}}$ is given, i.e., $\hat{a}_{2\nu_1+1,\nu_2}$ for $\nu_1 = -\frac{n}{2}, \ldots, \frac{n}{2} - 1$, $\nu_2 = -m, \ldots, m$. With this knowledge, we can recover the differences $a_{k_1,k_2} - a_{k_1+n,k_2}$ of the components in $\mathbf{A} = (a_{k_1,k_2})_{k_1=-n,k_2=-m}^{n-1,m-1}$ exactly for $k_1 = 0, \ldots, n-1$, $k_2 = -m, \ldots, m$, since

$$
\begin{aligned}
\tfrac{\sqrt{MN}}{2}(a_{k_1,k_2} - a_{k_1-n,k_2}) &= \tfrac{1}{2} \sum_{\nu_2=-m}^{m-1} \Big(\sum_{\nu_1=-n}^{n-1} \hat{a}_{\nu_1,\nu_2} (\omega_N^{-k_1\nu_1} - \omega_N^{-(k_1-n)\nu_1}) \Big) \omega_M^{-k_2\nu_2} \\
&= \tfrac{1}{2} \sum_{\nu_1=-n}^{n-1} \sum_{\nu_2=-m}^{m-1} \hat{a}_{\nu_1,\nu_2} (\omega_N^{-k_1\nu_1} - (-1)^{\nu_1}\omega_N^{-k_1\nu_1})\, \omega_M^{-k_2\nu_2} \\
&= \sum_{\nu_1=-n/2}^{n/2-1} \sum_{\nu_2=-m}^{m-1} \hat{a}_{2\nu_1+1,\nu_2} \omega_N^{-k_1(2\nu_1+1)} \omega_M^{-k_2\nu_2}. \qquad (2.1)
\end{aligned}
$$

Unfortunately, the remaining information needed to recover $\mathbf{A}$, namely the sums $(a_{k_1,k_2} + a_{k_1+n,k_2})$ for $k_1 = 0, \ldots, n-1$, $k_2 = -m, \ldots, m$, only depend on the non-acquired even-indexed Fourier data $\hat{a}_{2\nu_1,\nu_2}$, and cannot be reconstructed.

Let $\mathbf{W} = (\mathsf{w}_{\nu_1,\nu_2})_{\nu_1=-\frac{n}{2},\nu_2=-m}^{\frac{n}{2}-1,m-1} \in \mathbb{C}^{n\times M}$ be a matrix of arbitrary complex weights and $\check{\mathbf{W}} := (\check{\mathsf{w}}_{k_1,k_2})_{k_1=-\frac{n}{2},k_2=-m}^{\frac{n}{2}-1,m-1} = \sqrt{Mn}\,\mathbf{F}_n^{-1}\mathbf{W}\mathbf{F}_M^{-1}$ its $2D$ inverse Fourier transform multiplied with $\sqrt{Mn}$. Further, we define a periodic extension of these weights by assuming that $\mathsf{w}_{\nu_1+\ell_1 n,\nu_2+\ell_2 M} = \mathsf{w}_{\nu_1,\nu_2}$ for all $\ell_1, \ell_2 \in \mathbb{Z}$, $\nu_1 = -\frac{n}{2}, \ldots, \frac{n}{2} - 1$, $\nu_2 = -m, \ldots, m-1$. Similarly for $\check{\mathsf{w}}_{k_1,k_2}$ is assumed to be n periodic with respect to the first index k_1. We can actually prove the following theorem for any (non-adaptive) interpolation scheme.

Theorem 2.1 *Let $\mathbf{A} = (a_{k_1,k_2})_{k_1=-n,k_2=-m}^{n-1,m-1} \in \mathbb{C}^{N\times M}$, $\hat{\mathbf{A}} = (\hat{a}_{\nu_1,\nu_2})_{\nu_1=-n,\nu_2=-m}^{n-1,m-1} \in \mathbb{C}^{N\times M}$ its 2-D Fourier transform, and assume that half of the Fourier data, namely*

$$\hat{a}_{2\nu_1+1,\nu_2}, \qquad \nu_1 = -\tfrac{n}{2}, \ldots, \tfrac{n}{2} - 1,\ \nu_2 = -m, \ldots, m-1,$$

are acquired. Let $\mathbf{W} = (\mathsf{w}_{\nu_1,\nu_2})_{\nu_1=-\frac{n}{2},\nu_2=-m}^{\frac{n}{2}-1,m-1} \in \mathbb{C}^{n\times M}$ be a matrix of arbitrary complex weights as given above. Then, any interpolation scheme in the Fourier domain of the *form*

$$\begin{aligned}\hat{\hat{a}}_{2\nu_1+1,\nu_2} &:= \hat{a}_{2\nu_1+1,\nu_2} \\ \hat{\hat{a}}_{2\nu_1,\nu_2} &:= \sum_{\ell_1=-\frac{n}{2}}^{\frac{n}{2}-1} \sum_{\ell_2=-m}^{m-1} \mathsf{w}_{\nu_1-\ell_1,\nu_2-\ell_2}\, \hat{a}_{2\ell_1+1,\ell_2},\end{aligned} \tag{2.2}$$

for $\nu_1 = -\frac{n}{2}, \ldots, \frac{n}{2}-1$, $\nu_2 = -m, \ldots, m-1$, *leads to an image approximation* $\tilde{\mathbf{A}} = (\tilde{a}_{k_1,k_2})_{k_1=-n,k_2=m}^{n-1,m-1}$, *where*

$$\tilde{a}_{k_1,k_2} = \tfrac{1}{2}(1 + \check{\mathsf{w}}_{k_1,k_2}\, \omega_N^{k_1})(a_{k_1,k_2} - a_{k_1-n,k_2})$$

for all $k_1 = 0, \ldots, n-1$, $k_2 = -m, \ldots, m-1$.

Proof: Taking the interpolation scheme (2.2), it follows with (2.1) for the components of $\tilde{\mathbf{A}} = \mathbf{F}_N^{-1} \hat{\hat{\mathbf{A}}} \mathbf{F}_M^{-1}$ that

$$\begin{aligned}\tilde{a}_{k_1,k_2} &= \tfrac{1}{\sqrt{MN}} \Big(\sum_{\nu_1=-\frac{n}{2}}^{\frac{n}{2}-1} \sum_{\nu_2=-m}^{m-1} \hat{a}_{2\nu_1+1,\nu_2} \omega_N^{-k_1(2\nu_1+1)} \omega_M^{-k_2\nu_2} + \sum_{\nu_1=-\frac{n}{2}}^{\frac{n}{2}-1} \sum_{\nu_2=-m}^{m-1} \hat{\hat{a}}_{2\nu_1,\nu_2} \omega_N^{-2k_1\nu_1} \omega_M^{-k_2\nu_2} \Big) \\
&= \tfrac{1}{2}(a_{k_1,k_2} - a_{k_1-n,k_2}) + \tfrac{1}{\sqrt{MN}} \sum_{\nu_1=-\frac{n}{2}}^{\frac{n}{2}-1} \sum_{\nu_2=-m}^{m-1} \sum_{\ell_1=-\frac{n}{2}}^{\frac{n}{2}-1} \sum_{\ell_2=-m}^{m-1} \mathsf{w}_{\nu_1-\ell_1,\nu_2-\ell_2}\, \hat{a}_{2\ell_1+1,\ell_2} \omega_N^{-2k_1\nu_1} \omega_M^{-k_2\nu_2} \\
&= \tfrac{1}{2}(a_{k_1,k_2} - a_{k_1-n,k_2}) \\
&+ \tfrac{1}{\sqrt{MN}} \sum_{\ell_1=-\frac{n}{2}}^{\frac{n}{2}-1} \sum_{\ell_2=-m}^{m-1} \hat{a}_{2\ell_1+1,\ell_2}\, \omega_N^{-2\ell_1 k_1} \omega_M^{-\ell_2 k_2} \sum_{\nu_1=-\frac{n}{2}}^{\frac{n}{2}-1} \sum_{\nu_2=-m}^{m-1} \mathsf{w}_{\nu_1-\ell_1,\nu_2-\ell_2} \omega_N^{-2k_1(\nu_1-\ell_1)} \omega_M^{-k_2(\nu_2-\ell_2)} \\
&= \tfrac{1}{2}(a_{k_1,k_2} - a_{k_1-n,k_2}) + \tfrac{1}{\sqrt{MN}} \Big(\sum_{\ell_1=-\frac{n}{2}}^{\frac{n}{2}-1} \sum_{\ell_2=-m}^{m-1} \hat{a}_{2\ell_1+1,\ell_2} \omega_N^{-2\ell_1 k_1} \omega_M^{-\ell_2 k_2} \Big) \check{\mathsf{w}}_{k_1,k_2} \\
&= \tfrac{1}{2}(a_{k_1,k_2} - a_{k_1-n,k_2}) + \tfrac{1}{\sqrt{MN}} \check{\mathsf{w}}_{k_1,k_2}\, \omega_N^{k_1} \Big(\sum_{\ell_1=-\frac{n}{2}}^{\frac{n}{2}-1} \sum_{\ell_2=-m}^{m-1} \hat{a}_{2\ell_1+1,\ell_2} \omega_N^{-(2\ell_1+1)k_1} \omega_M^{-\ell_2 k_2} \Big) \\
&= \tfrac{1}{2}(1 + \check{\mathsf{w}}_{k_1,k_2}\, \omega_N^{k_1})(a_{k_1,k_2} - a_{k_1-n,k_2}),\end{aligned}$$

where $\check{\mathbf{W}} = (\check{\mathsf{w}}_{k_1,k_2})_{k_1=-\frac{n}{2},k_2=-m}^{\frac{n}{2}-1,m-1} = \sqrt{Mn}\mathbf{F}_N^{-1} \mathbf{W} \mathbf{F}_M$ as defined above. ∎

This observation shows that we are in fact unable to find a good reconstruction of an image only from the data in the set $\Lambda_{N/r,M}$, i.e., for the sampling pattern, where every second row of the image is missing. Any non-adaptive interpolation scheme does not get rid of the problem that we obtain just twice a (scaled) version of the difference of the upper and the lower half of the image. In other words, the low-pass set is crucial for the image reconstruction. Therefore, in the remaining sections, we always assume that $L = 2\ell + 1 > 0$, i.e., we have a certain low-pass part of the image which is completely acquired.

Remark 2.2 *Obviously, a similar observation as in Theorem* 2.1 *can be shown if instead of all odd-indexed rows of* $\hat{\mathbf{A}}$ *all even-indexed rows are acquired. Then, we have for* $k_1 = 0, \ldots, n-1$, $k_2 = -m, \ldots, m-1$,

$$a_{k_1,k_2} + a_{k_1-n,k_2} = \tfrac{2}{\sqrt{MN}} \sum_{\nu_1=-\frac{n}{2}}^{\frac{n}{2}-1} \sum_{\nu_2=-m}^{m-1} \hat{a}_{2\nu_1,\nu_2} \omega_N^{-2k_1\nu_1} \omega_M^{-k_2\nu_2},$$

and any interpolation scheme for the unacquired Fourier values of the form

$$\hat{\hat{a}}_{2\nu_1+1,\nu_2} := \sum_{\ell_1=-\frac{n}{2}}^{\frac{n}{2}-1} \sum_{\ell_2=-m}^{m-1} \mathsf{w}_{\nu_1-\ell_1,\nu_2-\ell_2}\, \hat{a}_{2\ell_1,\ell_2},\ \nu_1 = -\tfrac{n}{2}, \ldots, \tfrac{n}{2}-1,\ \nu_2 = -m, \ldots, m-1,$$

leads to a reconstruction $\tilde{\mathbf{A}}$*, where*

$$\tilde{a}_{k_1,k_2} = \tfrac{1}{2}(1 + \omega_N^{-k_1} \check{\mathsf{w}}_{k_1,k_2})(a_{k_1,k_2} + a_{k_1-n,k_2})$$

for all $k_1 = 0, \ldots, n-1$*,* $k_2 = -m, \ldots, m-1$*. In this case, we do not get rid of the factor* $(a_{k_1,k_2} + a_{k_1-n,k_2})$*.*

2.2 Zero refilling

The simplest approach to reconstruct $\mathbf{A}$ from the incomplete Fourier data $\mathbf{P}^{(\Lambda)} \circ \hat{\mathbf{A}}$ is to replace the missing Fourier data by zero before applying the inverse 2D Fourier transform, i.e.,

$$\tilde{\mathbf{A}}^{(z)} := \mathbf{F}_N^{-1}(\mathbf{P}^{(\Lambda)} \circ \hat{\mathbf{A}})\mathbf{F}_M^{-1}. \tag{2.3}$$

For the components of the zero refilling reconstruction $\tilde{\mathbf{A}}^{(z)}$ we obtain with $\mathbf{P}^{(\Lambda)} = (\mathbf{p}_{\boldsymbol{\nu}}^{(\Lambda)})_{\boldsymbol{\nu}\in\Lambda_{N,M}}$

$$\tilde{a}_{\mathbf{k}}^{(z)} = \frac{1}{\sqrt{MN}} \sum_{\boldsymbol{\nu}\in\Lambda_{N,M}} \mathbf{p}_{\boldsymbol{\nu}}^{(\Lambda)} \hat{a}_{\boldsymbol{\nu}}\, \omega_N^{-k_1\nu_1} \omega_M^{-k_1\nu_2} = a_{\mathbf{k}} + \frac{1}{\sqrt{MN}} \sum_{\boldsymbol{\nu}\in\Lambda_{N,M}} (\mathbf{p}_{\boldsymbol{\nu}}^{(\Lambda)} - 1)\, \hat{a}_{\boldsymbol{\nu}}\, \omega_N^{-k_1\nu_1} \omega_M^{-k_1\nu_2}$$

and the error can be written as

$$\|\tilde{\mathbf{A}}^{(z)} - \mathbf{A}\|_F^2 = \|\hat{\tilde{\mathbf{A}}}^{(z)} - \hat{\mathbf{A}}\|_F^2 = \frac{1}{\sqrt{MN}} \sum_{\boldsymbol{\nu}\notin\Lambda_{N,M}} |\hat{a}_{\boldsymbol{\nu}}|^2 = \sum_{\nu_1\notin\Lambda_1} \sum_{\nu_2=-m}^{m-1} |\hat{a}_{\nu_1,\nu_2}|^2$$

with Λ_1 in (1.4), i.e., the smaller the 2-norm of the vector consisting of all missing Fourier values, the smaller the reconstruction error. Obviously, if the non-acquired Fourier values are zero, then the error vanishes.

Let $\check{\mathbf{A}} := \mathbf{F}_N\mathbf{A} = \hat{\mathbf{A}}\mathbf{F}_M$, and denote with $\check{\mathbf{a}}_{k_2}$, $k_2 = -m, \ldots, m-1$, its columns. Further, let $\tilde{\mathbf{a}}_{k_2}^{(z)}$, $k_2 = -m, \ldots, m-1$, denote the columns of the reconstructed matrix $\tilde{\mathbf{A}}^{(z)}$ in (2.3). Then the reconstruction for every single column is of the form

$$\tilde{\mathbf{a}}_{k_2}^{(z)} = \mathbf{F}_N^{-1}(\mathbf{p}^{(\Lambda_1)} \circ \check{\mathbf{a}}_{k_2}), \quad k_2 = -m, \ldots, m-1,$$

where $\mathbf{p}^{(\Lambda_1)} \in \mathbb{R}^N$ has components 1 for indices in Λ_1 and zeros otherwise. Application of the discrete periodic convolution yields

$$\tilde{\mathbf{a}}_{k_2}^{(z)} = \mathbf{F}_N^{-1}\mathbf{p}^{(\Lambda_1)} \star \mathbf{F}_N^{-1}\check{\mathbf{a}}_{k_2} = \mathbf{F}_N^{-1}\mathbf{p}^{(\Lambda_1)} \star \mathbf{a}_{k_2} = \frac{1}{\sqrt{N}}\Big(\sum_{r\in\Lambda_1} \omega_N^{-rk_1}\Big)_{k_1=-n}^{n-1} \star \mathbf{a}_{k_2}.$$

This convolution can also be written as a matrix vector product with a circulant matrix

$$\tilde{\mathbf{a}}_{k_2}^{(z)} = \operatorname{circ}(\mathbf{F}_N^{-1}\mathbf{p}^{(\Lambda_1)})\mathbf{a}_{k_2} = \operatorname{circ}(\check{\mathbf{p}}^{(\Lambda_1)})\mathbf{a}_{k_2} = \big(\check{p}_{k_1-j_1}^{(\Lambda_1)}\big)_{k_1,j_1=-n}^{n-1} \mathbf{a}_{k_2},$$

where $\check{\mathbf{p}}^{(\Lambda_1)} = (\check{p}_k^{(\Lambda_1)})_{k=-n}^{n-1}$ with $\check{p}_k^{(\Lambda_1)} = \frac{1}{\sqrt{N}} \sum\limits_{r\in\Lambda_1} \omega_N^{rk}$. Thus,

$$\|\mathbf{a}_{k_2} - \tilde{\mathbf{a}}_{k_2}^{(z)}\|_2 = \big\|(\mathbf{I} - (\check{p}_{k_1-j_1}^{(\Lambda_1)})_{k_1,j_1=-n}^{n-1})\mathbf{a}_{k_2}\big\|_2 \le \big\|(\mathbf{I} - (\check{p}_{k_1-j_1}^{(\Lambda_1)})_{k_1,j_1=-n}^{n-1})\big\|_2 \|\mathbf{a}_{k_2}\|_2, \quad (2.4)$$

i.e., using the spectral norm of matrices, the relative error for the zero refilling reconstruction for arbitrary column vectors $\mathbf{a_k}$ can only be estimated by

$$\big\|(\mathbf{I}_N - (\check{p}_{k_1-j_1}^{(\Lambda_1)})_{k_1,j_1=-n}^{n-1})\big\|_2 = \|\mathbf{I}_N - \mathrm{diag}(\mathbf{p}^{(\Lambda_1)})\|_2 = 1.$$

Indeed, for matrices $\hat{\mathbf{A}}$ containing only high-pass components which are not acquired by the scheme, a reconstruction is not at all possible. However, natural images $\mathbf{A}$ usually possess some smoothness properties, which can in the discrete case be measured by local variations of pixel values. Therefore the acquired low-pass Fourier data contain a lot of information and the reduction rate r as well as the choice of the parameter L in the sampling set Λ in (1.1) become relevant.

For natural images, the special choice $\Lambda = \Lambda_{L,M}$ with $L = \lfloor \frac{N}{r} \rfloor$ (or $L = \lfloor \frac{N}{r} \rfloor - 1$ if $\lfloor \frac{N}{r} \rfloor$ is even), i.e., a sampling set consisting only of the centered low-pass set, is usually favourable for the application of zero refilling, see Figure 1. In this case, $\hat{\mathbf{p}}^{(\Lambda_1)} = \hat{\mathbf{p}}^{(\Lambda_L)}$ has the components $\sum_{j=-\ell}^{\ell} \omega_N^{jk}$, $k = -n, \ldots, n-1$, which are samples of the Dirichlet kernel $D_\ell(\omega) = \sum_{j=-\ell}^{\ell} \mathrm{e}^{\mathrm{i}\omega j}$.

The estimate (2.4) shows that a more general model, where the vector $\mathbf{p}^{(\Lambda_1)}$ (which only has components 1 or 0) is replaced by a vector $\mathbf{q}^{(\Lambda_1)}$ with arbitrary nonzero components for indices in Λ_1, cannot reduce the 2-error for arbitrary signals. However, the aliasing effects, which always occur for reconstruction with the Dirichlet window, can be reduced by taking other window functions, as e.g. the Hamming window, which is defined by $\check{\mathbf{p}}^{(Ham)} = \mathbf{F}_N^{-1}\mathbf{p}^{(Ham)}$ with $\mathbf{p}^{(Ham)} = (p_k)_{k=-n}^{n-1}$, where

$$p_k^{(Ham)} := \begin{cases} 0.54 + 0.46\cos(\frac{2\pi k}{2\ell}) & -\ell \le k \le \ell. \\ 0 & \text{otherwise.} \end{cases}$$

While the application of the Hamming window instead of the Dirichlet window avoids the special ringing artefacts, we observe a strong oversmoothing. Figure 2 shows zero refilling reconstructions of the 512×512 pepper image for reduction rate $r = 6$ and with $L = 85 = \lfloor \frac{512}{6} \rfloor - 1$, i.e., $\Lambda_1 = \Lambda_L = \{-42, \ldots, 42\}$ (Dirichlet window $\mathbf{p}^{(\Lambda_1)}$), for $r = 6$ and $L = 85$, with the Hamming window $\mathbf{p}^{(Ham)}$, and for the sampling set Λ in (1.1) with $r = 6$ and $L = 43$. The bottom row shows the corresponding window vectors $\check{\mathbf{p}}^{(\Lambda_L)}$, $\check{\mathbf{p}}^{(Ham)}$ and $\check{\mathbf{p}}^{\Lambda_1}$, which are approximations of the ideal window $(\delta_{0,k})_{k=-n}^{n-1}$ that we would obtain for complete Fourier data. In Theorem 2.1 we had shown that for $L = 0$, a non-adaptive scheme always leads to a reconstruction, where $\tilde{a}_{k_1,k_2}$ contains the factor $a_{k_1,k_2} - a_{k_1-n,k_2}$ for all $k_1 = 0, \ldots, n-1$, $k_2 = -m, \ldots, m$. This effect is only partially reduced by employing a low-pass set $\Lambda_{L,M}$ with $L > 0$, see Figure 2 (right).

Using the flexibility of the sampling set Λ in (1.1), where we can fix the width $L \in \{0, \ldots, \lfloor \frac{N}{r} \rfloor\}$ of the low-pass set, we are interested in data-adaptive algorithms that essentially improve the recovery results achieved by low-pass reconstruction using zero refilling.

2.3 Non-adaptive reconstruction approach

Next we shortly show, why a non-data-adaptive reconstruction approach does generally not yield recovery results which outperform the simple zero refilling procedure.

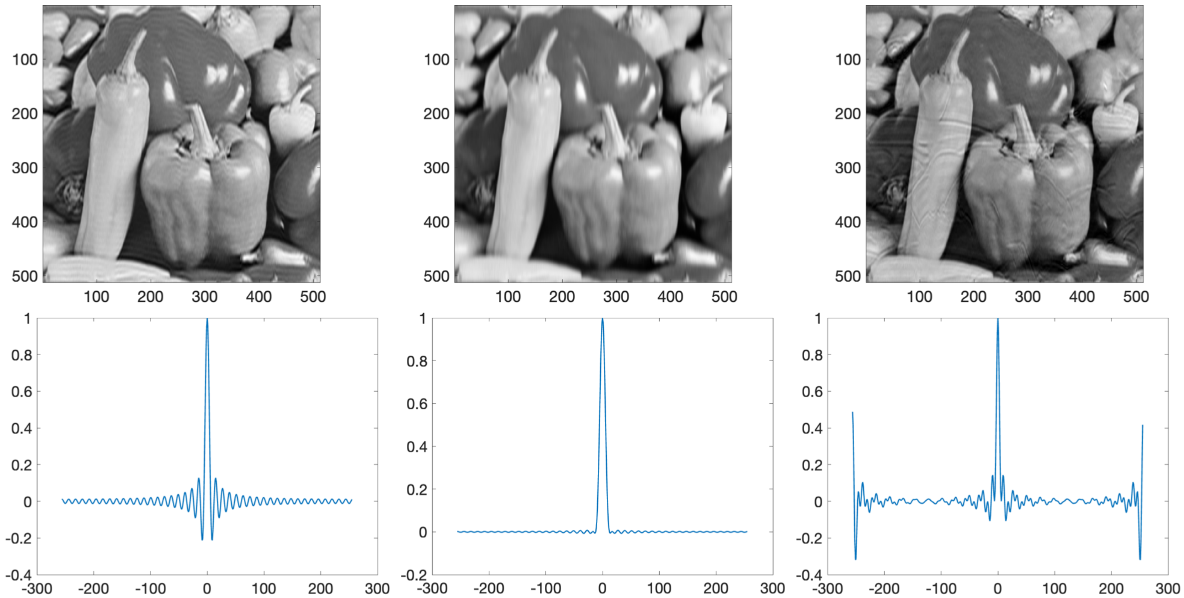

Figure 2: Top: Reconstructions of the 512×512 pepper image. Left: Approximation with Dirichlet window using $L = \lfloor 512/r \rfloor = 85$ for $r = 6$ with PSNR 28.21; Middle: Approximation with Hamming window with $L = \lfloor 512/r \rfloor = 85$ for $r = 6$ with PSNR 25.57; Right: Reconstruction by zero refilling with reduction rate $r = 6$ and $L = 43$ with PSNR 26.75. Bottom: Corresponding representations of the windows $\check{\mathbf{p}}^{(\Lambda_L)}$ for $r = 6$, $L = 85$, $\check{\mathbf{p}}^{(Ham)}$ for $r = 6$, $L = 85$ (middle), and $\check{\mathbf{p}}^{(\Lambda_1)}$ for $r = 6$, $L = 43$

Recall that we want to find an optimal approximation $\tilde{\mathbf{A}}$ of $\mathbf{A}$ from $\mathbf{P}^{(\Lambda)} \circ \hat{\mathbf{A}}$. Equivalently, we need to approximate the non-acquired Fourier data to get an optimal approximation $\hat{\tilde{\mathbf{A}}}$ from $\mathbf{P}^{(\Lambda)} \circ \hat{\mathbf{A}}$.

Using a model based on a linear transform, we can rewrite the problem in a vectorized form as follows: Find a matrix $\mathbf{Q} \in \mathbb{C}^{NM \times NM}$ to recover $\mathrm{vec}(\tilde{\mathbf{A}})$ by

$$\mathrm{vec}(\hat{\tilde{\mathbf{A}}}) = \mathbf{Q}\,(\mathrm{vec}(\mathbf{P}^{(\Lambda)}) \circ \mathrm{vec}(\hat{\mathbf{A}})) = \mathbf{Q}\,\mathrm{diag}(\mathrm{vec}(\mathbf{P}^{(\Lambda)}))\mathrm{vec}(\hat{\mathbf{A}})$$

such that

$$\begin{aligned}\|\mathrm{vec}(\mathbf{A}) - \mathrm{vec}(\tilde{\mathbf{A}})\|_2 = \|\mathrm{vec}(\hat{\mathbf{A}}) - \mathrm{vec}(\hat{\tilde{\mathbf{A}}})\|_2 &= \|\mathrm{vec}(\hat{\mathbf{A}}) - \mathbf{Q}\,\mathrm{diag}(\mathrm{vec}(\mathbf{P}^{(\Lambda)}))\mathrm{vec}(\hat{\mathbf{A}})\|_2 \\ &= \|(\mathbf{I} - \mathbf{Q}\,\mathrm{diag}(\mathrm{vec}(\mathbf{P}^{(\Lambda)})))\mathrm{vec}(\hat{\mathbf{A}})\|_2\end{aligned}$$

is minimized for arbitrary matrices $\hat{\mathbf{A}}$. Note that this model includes any non-adaptive interpolation scheme to approximate the missing components of $\hat{\mathbf{A}}$. Taking the Frobenius norm for matrices, it follows that $\|\mathbf{I} - \mathbf{Q}\,\mathrm{diag}(\mathrm{vec}(\mathbf{P}^{(\Lambda)}))\|_F$ has to be minimized. Denote the components of $\mathbf{Q}$ by $q_{\mathbf{k},\boldsymbol{\ell}}$, $\mathbf{k}, \boldsymbol{\ell} \in \Lambda_{N,M}$, and the diagonal elements of $\mathrm{diag}(\mathrm{vec}(\mathbf{P}^{(\Lambda)}))$ by $p_{\boldsymbol{\ell}}^{(\Lambda)}$. Separating the diagonal and the non-diagonal entries, we obtain

$$\begin{aligned}\|\mathbf{I}_{MN} - \mathbf{Q}\,\mathrm{diag}(\mathrm{vec}(\mathbf{P}^{(\Lambda)}))\|_F^2 &= \sum_{\mathbf{k},\boldsymbol{\ell} \in \Lambda_{N,M}} |\delta_{\mathbf{k},\boldsymbol{\ell}} - q_{\mathbf{k},\boldsymbol{\ell}}\, p_{\boldsymbol{\ell}}^{(\Lambda)}|^2 + \\ &= \sum_{\boldsymbol{\ell} \in \Lambda} |1 - q_{\boldsymbol{\ell},\boldsymbol{\ell}}|^2 + (NM - |\Lambda|) + \sum_{\boldsymbol{\ell} \in \Lambda} \sum_{\substack{\mathbf{k} \in \Lambda_{N,M} \\ \mathbf{k} \neq \boldsymbol{\ell}}} |q_{\mathbf{k},\boldsymbol{\ell}}|^2, \qquad (2.5)\end{aligned}$$

where $(NM - |\Lambda|)$ is the number on non-acquired Fourier components. Obviously, (2.5) is minimized for $\mathbf{Q} = \mathrm{diag}(\mathrm{vec}(\mathbf{P}^{(\Lambda)}))$, since then the first and the last sum vanish. The matrix $\mathbf{Q} = \mathrm{diag}(\mathrm{vec}(\mathbf{P}^{(\Lambda)})$ is also an optimal solution if the Frobenius norm in (2.5) is replaced by the spectral norm. Thus, regarding these norms, there is no better nonadaptive solution than the reconstruction by zero refilling.

2.4 Low-rank approximation

For matrix completion problems, often a low-rank constraint has been successfully employed. We shortly explain, why a low-rank constraint is unfortunately not helpful to solve our problem of image recovery from structured incomplete Fourier data.

Let $\tilde{\mathbf{A}}$ denote the wanted image reconstruction, where we assume that the given constraint $\mathbf{P}^{(\Lambda)} \circ \hat{\tilde{\mathbf{A}}} = \mathbf{P}^{(\Lambda)} \circ \hat{\mathbf{A}}$ is satisfied. Then, we observe that the solution $\tilde{\mathbf{A}}^{(z)}$ in (2.3), obtained by zero refilling, already satisfies

$$\mathrm{rank}(\tilde{\mathbf{A}}^{(z)}) = \mathrm{rank}(\mathbf{F}_N^{-1}(\mathbf{P}^{(\Lambda)} \circ \hat{\mathbf{A}})\mathbf{F}_M^{-1}) = \mathrm{rank}(\mathbf{P}^{(\Lambda)} \circ \hat{\mathbf{A}}) \leq \tfrac{N}{r}$$

since at most $\frac{N}{r}$ rows of $\mathbf{P}^{(\Lambda)} \circ \hat{\mathbf{A}}$ are non-zero rows. Thus, if we request for $\tilde{\mathbf{A}}$ a low rank being larger than or equal to $\mathrm{rank}(\mathbf{P}^{(\Lambda)} \circ \hat{\mathbf{A}})$, we obtain the solution $\tilde{\mathbf{A}}^{(z)}$ in (2.3), while for requesting a smaller rank, the Fourier constraints can no longer be satisfied exactly. Therefore the low-rank constraint seems not to be well applicable.

2.5 Locally adaptive interpolation in Fourier domain

As we have seen in Theorem 2.1, interpolation in the absence of a low-pass set is futile, which is why many Fourier reconstruction methods (especially in the field of MRI) use a low-pass set. The quality of the reconstruction strongly depends on the size of this set, located at the center of the Fourier space. As before, let $\hat{\mathbf{A}} = (\hat{a}_{\boldsymbol{\nu}})_{\boldsymbol{\nu} \in \Lambda_{N,M}}$ be the 2D DFT of $\mathbf{A}$ and $\mathbf{P}^{\Lambda} \circ \hat{\mathbf{A}}$ the acquired Fourier data with Λ in (1.1).

Some Fourier interpolation methods in MRI, like GRAPPA [10] and SPIRiT [19], use the fully sampled low-pass area to learn interpolation weights to reconstruct the remaining data in Fourier domain.

Remark 2.3 *Note that MRI interpolation methods like GRAPPA and SPIRiT make use of different coils that gather Fourier data (so-called k-space data in MRI) in parallel, something that is absent from our model. Therefore, our reconstruction problem can be regarded as a special case of GRAPPA and SPIRiT with only one coil.*

The main idea of these methods is to determine suitable weights for a local interpolation scheme in the first step and then to apply these weights to reconstruct the missing Fourier data. We shortly summarize these two methods for our sampling scheme, which are heavily used in MRI reconstructions.

We start with the idea of the GRAPPA interpolation [10]. Here the structure of the sampling scheme for the acquired Fourier data is directly employed to find the weights from the low-pass area, where all Fourier data are given. Let $\mathcal{N}$ be a small centered index set (window), e.g. $\mathcal{N} = \{-p_1, \ldots, p_1\} \times \{-p_2, \ldots, p_2\}$ with $p_1, p_2 \in \mathbb{N}$ and with $|\mathcal{N}| = (2p_1 + 1)(2p_2 + 1)$ indices.

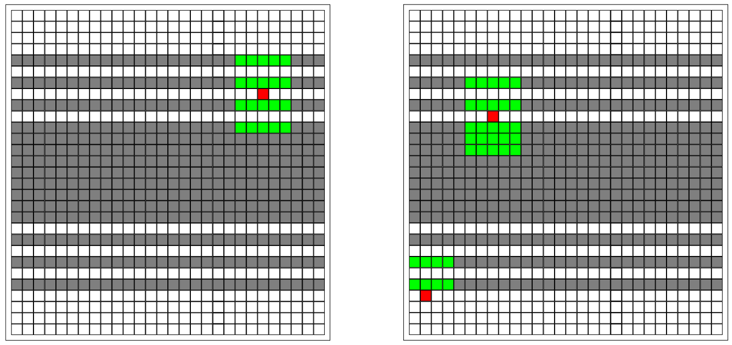

Figure 3: Example for different patterns $\mathcal{P}$ for GRAPPA interpolation using local interpolation in a 7×5 window. All gray- and green-valued pixel values are acquired. Green pixel values are employed to interpolate the red pixel value

Using the sampling structure given by $\mathbf{P}^{\Lambda}$ in (1.3) with Λ in (1.1), a local interpolation scheme for unacquired data $\hat{a}_{\boldsymbol{\nu}}$, $\boldsymbol{\nu} \in \Lambda_{N,M} \setminus \Lambda$, is taken in the form

$$\hat{\hat{a}}_{\boldsymbol{\nu}} = \sum_{\substack{\mathbf{j} \in \mathcal{N} \\ \boldsymbol{\nu}+\mathbf{j} \in \Lambda}} g_{\mathbf{j}} \, \hat{a}_{\boldsymbol{\nu}+\mathbf{j}} = \sum_{\mathbf{j} \in \mathcal{P}(\boldsymbol{\nu})} g_{\mathbf{j}} \, \hat{a}_{\boldsymbol{\nu}+\mathbf{j}} \tag{2.6}$$

for all components $\boldsymbol{\nu}$ in non-acquired rows of $\hat{\mathbf{A}}$, where on the right-hand side only the acquired values with indices in the window $\boldsymbol{\nu} + \mathcal{N}$ come into play. The index set $\mathcal{P}(\boldsymbol{\nu}) := \{\mathbf{j} \in \mathcal{N}, \, \mathbf{j} + \boldsymbol{\nu} \in \Lambda\}$ depends on the location of $\boldsymbol{\nu}$. Figure 3 illustrates different index sets $\mathcal{P}(\boldsymbol{\nu})$ (green) around the index $\boldsymbol{\nu}$ of an unacquired pixel value (red).

Depending on the location of the pixel values that one wants to recover, a certain number of different patterns $\mathcal{P} = \mathcal{P}(\boldsymbol{\nu})$ of acquired neighboring pixel values occurs. Employing the given Fourier values in the low-pass area, for every occurring pattern $\mathcal{P} \subset \mathcal{N}$ the weights $(g_{\mathbf{j}})_{\mathbf{j} \in \mathcal{P}} = (g_{\mathbf{j}}^{(\mathcal{P})})_{\mathbf{j} \in \mathcal{P}}$ are assumed to satisfy

$$\hat{a}_{\boldsymbol{\nu}} = \sum_{\mathbf{j} \in \mathcal{P}} g_{\mathbf{j}}^{(\mathcal{P})} \, \hat{a}_{\boldsymbol{\nu}+\mathbf{j}} \qquad \text{for all}\, \boldsymbol{\nu} \in \Lambda_{L,M} \;\text{ with }\; \boldsymbol{\nu} + \mathcal{P} \in \Lambda_{L,M}. \tag{2.7}$$

We denote the set of indices $\boldsymbol{\nu}$ with $\boldsymbol{\nu} + \mathcal{P} \in \Lambda_{L,M}$ by $\Lambda_{L,M}^{(\mathcal{P})}$. The weights $g_{\mathbf{j}} = g_{\mathbf{j}}^{(\mathcal{P})}$ are then determined by solving the least squares problem emerging from the equations in (2.7). We vectorize (columnwise) and obtain with

$$\begin{aligned} \hat{\mathbf{a}}^{(cal,\mathcal{P})} &:= (\hat{a}_{\boldsymbol{\nu}})_{\boldsymbol{\nu} \in \Lambda_{L,M}^{(\mathcal{P})}} \in \mathbb{C}^{|\Lambda_{L,M}^{(\mathcal{P})}|}, \quad \hat{\mathbf{A}}_{\mathcal{P}} := (\hat{a}_{\boldsymbol{\nu}+\mathbf{j}})_{\boldsymbol{\nu} \in \Lambda_{L,M}^{(\mathcal{P})}, \mathbf{j} \in \mathcal{P}} \in \mathbb{C}^{|\Lambda_{L,M}^{(\mathcal{P})}| \times |\mathcal{P}|}, \\ \mathbf{g}^{(\mathcal{P})} &:= (g_{\mathbf{j}}^{(\mathcal{P})})_{\mathbf{j} \in \mathcal{P}} \in \mathbb{C}^{|\mathcal{P}|} \end{aligned}$$

the least squares problem

$$\mathbf{g}^{(\mathcal{P})} \quad = \operatorname*{argmin}_{\tilde{\mathbf{g}}} \|\hat{\mathbf{a}}^{(cal,\mathcal{P})} - \hat{\mathbf{A}}_{\mathcal{P}} \, \tilde{\mathbf{g}}\|_2 \tag{2.8}$$

to determine $\mathbf{g}^{(\mathcal{P})}$. All unacquired pixel values $\hat{\mathbf{a}}_{\boldsymbol{\nu}}$ with larger row index, whose $\mathcal{N}$ neighborhood does not contain acquired values, stay to be filled with zeros, since we have no neighbour information about these values.

Remark 2.4 *In the original paper [10], it is proposed to use several interpolation schemes with small windows, which need not to be centered, and to apply an averaging procedure in the end.*

In [19], a different procedure is proposed. Again, it is assumed that the Fourier data $\hat{a}_{\boldsymbol{\nu}}$ can be approximated by a suitable linear combination of neighboring Fourier data with indices in a small window $\boldsymbol{\nu} + \mathcal{N}$. This time, an interpolation scheme for all data, regardless of being acquired or not, is derived and later taken as a constraint in a minimization problem to recover the missing data. Using periodic boundary conditions, the weights are supposed to satisfy the constraints

$$\hat{a}_{\boldsymbol{\nu}} = \sum_{\mathbf{j} \in \mathcal{N} \setminus \{\mathbf{0}\}} g_{\mathbf{j}} \, \hat{a}_{\boldsymbol{\nu}+\mathbf{j}} = \sum_{\mathbf{j}' \in \Lambda_{N,M}} g_{\mathbf{j}'-\boldsymbol{\nu}} \, \hat{a}_{\mathbf{j}'}, \qquad \boldsymbol{\nu} \in \Lambda_{M,N}, \tag{2.9}$$

where we assume that $g_{\mathbf{j}} = 0$ for $\mathbf{j} \notin \mathcal{N} \setminus \{\mathbf{0}\}$ and $\boldsymbol{\nu} + \mathbf{j} = \boldsymbol{\nu} + \mathbf{j} \bmod \Lambda_{N,M}$, $\mathbf{j}' - \boldsymbol{\nu} = \mathbf{j}' - \boldsymbol{\nu} \bmod \Lambda_{N,M}$. In a first step, the weights $g_{\mathbf{j}}$, $\mathbf{j} \in \mathcal{N} \setminus \{\mathbf{0}\}$, are computed from the given data in the low-pass area similarly as in (2.8). We use the notation $\Lambda_{L,M}^{(\mathcal{N})}$ for the set of indices $\boldsymbol{\nu}$ with $\boldsymbol{\nu} + \mathcal{N} \in \Lambda_{L,M}$. Then we obtain after vectorization with $\hat{\mathbf{a}}^{(cal,\mathcal{N})} := (\hat{a}_{\boldsymbol{\nu}})_{\boldsymbol{\nu} \in \Lambda_{L,M}^{(\mathcal{N})}}$ and $\hat{\mathbf{A}}_{\mathcal{N}} := (\hat{a}_{\boldsymbol{\nu}+\mathbf{j}})_{\boldsymbol{\nu} \in \Lambda_{L,M}^{(\mathcal{N})}, \mathbf{j} \in \mathcal{N} \setminus \{\mathbf{0}\}}$ the linear least squares problem

$$\mathbf{g}_0 = \operatorname*{argmin}_{\tilde{\mathbf{g}}} \|\hat{\mathbf{a}}^{(cal,\mathcal{N})} - \hat{\mathbf{A}}_{\mathcal{N}} \, \tilde{\mathbf{g}}\|_2^2,$$

where $\mathbf{g}_0 = (g_{\mathbf{j}})_{\mathbf{j} \in \mathcal{N} \setminus \{\mathbf{0}\}} \in \mathbb{C}^{|\mathcal{N}|-1}$. If the weights satisfy (2.9) for all $\boldsymbol{\nu} \in \Lambda_{M,N}$, one can conclude that

$$\operatorname{vec}(\hat{\mathbf{A}}) = \mathbf{G} \operatorname{vec}(\hat{\mathbf{A}}), \tag{2.10}$$

where $\mathbf{G} := (g_{\mathbf{j}-\boldsymbol{\nu}})_{\boldsymbol{\nu} \in \Lambda_{N,M}, \mathbf{j} \in \Lambda_{M,N}}$ is a (sparse) block Toeplitz matrix. To find an approximation $\hat{\tilde{\mathbf{A}}}$ of $\hat{\mathbf{A}}$, one considers in [19] an optimization problem of the form

$$\min_{\tilde{\mathbf{A}}} \Big(\|\mathbf{P}^{\Lambda} \circ (\hat{\tilde{\mathbf{A}}} - \hat{\mathbf{A}})\|_F^2 + \lambda \|(\mathbf{G} - \mathbf{I}_{MN}) \operatorname{vec}(\hat{\tilde{\mathbf{A}}})\|_2^2 \Big), \tag{2.11}$$

where the first term takes care of the approximation of the given Fourier values and the second ensures (2.10). The first term has the vectorized form $\|(\mathbf{I}_M \otimes \operatorname{diag}(\mathbf{p}^{\Lambda_1}))(\operatorname{vec}(\hat{\tilde{\mathbf{A}}}) - \operatorname{vec}(\hat{\mathbf{A}}))\|_2^2$. The minimization problem (2.11) can be directly solved. Calculating the gradient with respect to $\operatorname{vec}(\hat{\tilde{\mathbf{A}}})$, we obtain the large linear system

$$\Big((\mathbf{I}_M \otimes \operatorname{diag}(\mathbf{p}^{\Lambda_1})) + \lambda (\mathbf{G} - \mathbf{I}_{MN})^* (\mathbf{G} - \mathbf{I}_{MN}) \Big) \operatorname{vec}(\hat{\tilde{\mathbf{A}}}) = 2 (\mathbf{I}_M \otimes \operatorname{diag}(\mathbf{p}^{\Lambda_1})) \operatorname{vec}(\hat{\mathbf{A}}).$$

This system can be iteratively solved using the fixed-point formulation

$$\begin{aligned} \operatorname{vec}(\hat{\tilde{\mathbf{A}}})_{n+1} = \operatorname{vec}(\hat{\tilde{\mathbf{A}}})_n - \mu \Big(& (\mathbf{I}_M \otimes \operatorname{diag}(\mathbf{p}^{\Lambda_1}))(\operatorname{vec}(\hat{\tilde{\mathbf{A}}})_n - \operatorname{vec}(\hat{\mathbf{A}})) \\ & + \lambda (\mathbf{G} - \mathbf{I}_{MN})^* (\mathbf{G} - \mathbf{I}_{MN}) \operatorname{vec}(\hat{\tilde{\mathbf{A}}})_n \Big) \end{aligned}$$

which converges if $\mu > 0$ is taken small enough.

Unfortunately, the two interpolation methods presented in the section usually do not provide satisfying reconstruction results in our setting compared to zero refilling and compared to the further recovering algorithms that we will consider in the next two sections. This is not surprising, if we look back at our results in Theorem 2.1 and Section 2.3, since adaptivity only relies here to the data in the low-pass area and the 2D DFT data usually do not possess small total variation that would ensure a good approximation by local interpolation.

3 Reconstruction by TV functional minimization

In this section we want to adapt a technique to our setting which is often used in image denoising and image reconstruction, namely the application of a regularizer based on minimizing the total variation. In contrast to other approaches based on TV regularization using randomly sampled measurements [4] or Fourier measurements on a polar grid [2, 27, 15], our 2D-DFT measurements are acquired on the the sampling pattern Λ in (1.1). We will adapt the primal-dual algorithm of Chambolle and Pock [6, 7] to minimize the obtained functional, where in our case one of the fixed-point iterations is performed in Fourier domain. We assume that the image $\mathbf{A}$ is real-valued, otherwise we reconstruct here the real and imaginary part of the $\mathbf{A}$ separately.

We start with some notations. Let

$$\mathbf{D}_N := \begin{pmatrix} -1 & 1 & & & \\ & -1 & 1 & & \\ & & \ddots & \ddots & \\ & & & -1 & 1 \\ & & & & 0 \end{pmatrix} \in \mathbb{R}^{N\times N} \tag{3.1}$$

denote the difference matrix, then the discrete gradient of $\mathbf{A} \in \mathbb{R}^{N\times M}$ is defined as $\nabla : \mathbb{R}^{N\times M} \to \mathbb{R}^{2N\times M}$,

$$\nabla(\mathbf{A}) := \begin{pmatrix} \mathbf{D}_N\mathbf{A} \\ \mathbf{A}\ \mathbf{D}_M^T \end{pmatrix}.$$

For $\mathbf{A} = (a_{\mathbf{k}})_{\mathbf{k}\in\Lambda_{N,M}} \in \mathbb{R}^{N\times M}$ and $\mathbf{B} = (b_{\mathbf{k}})_{\mathbf{k}\in\Lambda_{N,M}} \in \mathbb{R}^{N\times M}$ let

$$\|\mathbf{A}\|_1 := \sum_{\mathbf{k}\in\Lambda_{N,M}} |a_{\mathbf{k}}|, \quad \langle \mathbf{A}, \mathbf{B}\rangle := \sum_{\mathbf{k}\in\Lambda_{N,M}} a_{\mathbf{k}} b_{\mathbf{k}}.$$

Further, for for $\mathbf{X} = \begin{pmatrix} \mathbf{X}_1 \\ \mathbf{X}_2 \end{pmatrix} \in \mathbb{R}^{2N\times M}$ with $\mathbf{X}_1 = (x_{\mathbf{k},1})_{\mathbf{k}\in\Lambda_{N,M}}$, $\mathbf{X}_2 = (x_{\mathbf{k},2})_{\mathbf{k}\in\Lambda_{N,M}}$ we define

$$\|\mathbf{X}\|_\infty := \max_{\mathbf{k}\in\Lambda_{N,M}} \sqrt{x_{\mathbf{k},1}^2 + x_{\mathbf{k},2}^2}. \tag{3.2}$$

To find a good image reconstruction $\tilde{\mathbf{A}}$ from the incomplete data $\mathbf{P}^{(\Lambda)}\hat{\mathbf{A}}$ in (1.3) our goal is to compute the minimizer of the functional

$$\min_{\tilde{\mathbf{A}}\in\mathbb{R}^{N\times M}} \Big(\tfrac{\lambda}{2} \|\mathbf{P}^{(\Lambda)} \circ (\hat{\tilde{\mathbf{A}}} - \hat{\mathbf{A}})\|_F^2 + \|\nabla(\tilde{\mathbf{A}})\|_1 \Big). \tag{3.3}$$

The regularization term $\|\nabla(\tilde{\mathbf{A}})\|_1$ is called the discrete total variation of $\tilde{\mathbf{A}}$. The regularization parameter λ has to be taken large in order to ensure that $\|\mathbf{P}^{(\Lambda)} \circ (\hat{\tilde{\mathbf{A}}} - \hat{\mathbf{A}})\|_F^2$ is very small.

As in [6], this problem is first transferred into a saddle-point problem. For this purpose, we introduce the mappings $G : \mathbb{R}^{M\times N} \to \mathbb{R}$ and $H : \mathbb{R}^{2N\times M} \to \mathbb{R}$ given by

$$G(\tilde{\mathbf{A}}) := \tfrac{\lambda}{2}\|\mathbf{P}^{(\Lambda)} \circ (\hat{\tilde{\mathbf{A}}} - \hat{\mathbf{A}})\|_F^2, \qquad H(\mathbf{C}) := \|\mathbf{C}\|_1, \qquad \tilde{\mathbf{A}} \in \mathbb{R}^{N\times M}, \quad \mathbf{C} \in \mathbb{R}^{2N\times M},$$

such that (3.3) can shortly be written $\min\limits_{\tilde{\mathbf{A}}\in\mathbb{R}^{N\times M}} (H(\nabla\tilde{\mathbf{A}}) + G(\tilde{\mathbf{A}}))$. With $H^* : \mathbb{R}^{2N\times M} \to \mathbb{R}$ we denote the convex conjugate of the convex function H,

$$H^*(\mathbf{X}) := \max_{\mathbf{C}\in\mathbb{R}^{2N\times M}} \Big(\langle \mathbf{X}, \mathbf{C}\rangle - H(\mathbf{C})\Big).$$

In our case we obtain

$$H^*(\mathbf{X}) = \max_{\mathbf{C}\in\mathbb{R}^{2N\times M}} \Big(\langle \mathbf{X}, \mathbf{C}\rangle - \|\mathbf{C}\|_1\Big) = \begin{cases} 0 & \text{if } \|\mathbf{X}\|_\infty \le 1, \\ +\infty & \text{otherwise,} \end{cases} \tag{3.4}$$

with $\|\mathbf{X}\|_\infty$ as in (3.2), see also [6]. The Fenchel-Moreau theorem, see e.g. [3], implies that $H^{**} = H$. Therefore, with $\mathbf{C} = \nabla(\tilde{\mathbf{A}})$ we also have

$$H(\mathbf{C}) = H(\nabla(\tilde{\mathbf{A}})) = \|\nabla(\tilde{\mathbf{A}})\|_1 = \max_{\mathbf{X}\in\mathbb{R}^{2N\times M}} \Big(\langle \nabla(\tilde{\mathbf{A}}), \mathbf{X}\rangle - H^*(\mathbf{X})\Big),$$

and (3.3) can equivalently be written as a saddle-point problem

$$\max_{\mathbf{X}\in\mathbb{R}^{2N\times M}} \min_{\tilde{\mathbf{A}}\in\mathbb{R}^{N\times M}} \Big(G(\tilde{\mathbf{A}}) + \langle \nabla(\tilde{\mathbf{A}}), \mathbf{X}\rangle - H^*(\mathbf{X})\Big). \tag{3.5}$$

Taking the subgradients with respect to $\mathbf{X}$ and $\tilde{\mathbf{A}}$, it follows that any solution $(\mathbf{X}, \tilde{\mathbf{A}})$ of (3.5) necessarily satisfies $\mathbf{0} \in \Big(\nabla(\tilde{\mathbf{A}}) - \partial H^*(\mathbf{X})\Big)$ and $\mathbf{0} \in \Big(\nabla^*(\mathbf{X}) + \partial G(\tilde{\mathbf{A}})\Big)$, i.e.,

$$\nabla(\tilde{\mathbf{A}}) \in \partial H^*(\mathbf{X}), \qquad -\nabla^*(\mathbf{X}) \in \partial G(\tilde{\mathbf{A}}). \tag{3.6}$$

Here, ∇^* is defined by $\langle \tilde{\mathbf{A}}, \nabla^*(\mathbf{X})\rangle = \langle \nabla(\tilde{\mathbf{A}}), \mathbf{X}\rangle$, i.e., $\nabla^*(\mathbf{X}) = \mathbf{D}_N\mathbf{X}_1 + \mathbf{X}_2\mathbf{D}_M^T$. The first condition in (3.6) yields by multiplying with a constant $\sigma > 0$ and adding $\mathbf{X}$ at both sides

$$\mathbf{X} + \sigma\nabla(\tilde{\mathbf{A}}) \in \mathbf{X} + \sigma\partial H^*(\mathbf{X}) = (\mathbf{I} + \sigma\partial H^*)(\mathbf{X}),$$

where $\mathbf{I}$ denotes the identity operator. Applying a similar procedure to the second condition in (3.6) with $\tau > 0$, we arrive at the two fixed-point equations,

$$\mathbf{X} = (\mathbf{I} + \sigma\partial H^*)^{-1}(\mathbf{X} + \sigma\nabla(\tilde{\mathbf{A}})), \tag{3.7}$$
$$\tilde{\mathbf{A}} = (\mathbf{I} + \tau\partial G)^{-1}(\tilde{\mathbf{A}} - \nabla^*(\mathbf{X})). \tag{3.8}$$

The primal-dual algorithm introduced in [6], which we adapt here to our setting, is based on alternating application of the two corresponding fixed-point iterations for the primal variable $\tilde{\mathbf{A}}$ and the dual variable $\mathbf{X}$.

Lets have now a closer look at the two resolvent operators (or proximity operators) $(\mathbf{I}+\sigma\partial H^*)^{-1}$ and $(\mathbf{I}+\tau\partial G)^{-1}$ occurring in (3.7)-(3.8). These are given by

$$(\mathbf{I}+\sigma\partial H^*)^{-1}(\mathbf{X}) := \operatorname*{argmin}_{\mathbf{Y}\in\mathbb{R}^{2N\times M}} \Big(\tfrac{1}{2\sigma}\|\mathbf{X}-\mathbf{Y}\|_F^2 + H^*(\mathbf{Y})\Big),$$
$$(\mathbf{I}+\tau\partial G)^{-1}(\tilde{\mathbf{A}}) := \operatorname*{argmin}_{\mathbf{Z}\in\mathbb{R}^{N\times M}} \Big(\tfrac{1}{2\tau}\|\tilde{\mathbf{A}}-\mathbf{Z}\|_F^2 + G(\mathbf{Z})\Big).$$

Indeed, for $\tilde{\mathbf{Y}} = \operatorname*{argmin}_{\mathbf{Y}\in\mathbb{R}^{2N\times M}} \Big(\tfrac{1}{2\sigma}\|\mathbf{X}-\mathbf{Y}\|_F^2 + H^*(\mathbf{Y})\Big)$ it follows

$$\mathbf{0} \in \partial\Big(\tfrac{1}{2\sigma}\|\mathbf{X}-\tilde{\mathbf{Y}}\|_F^2 + H^*(\tilde{\mathbf{Y}})\Big) = \tfrac{1}{\sigma}(\tilde{\mathbf{Y}}-\mathbf{X}) + \partial H^*(\tilde{\mathbf{Y}}),$$

i.e., $\mathbf{X} \in \tilde{\mathbf{Y}} + \sigma\partial H^*(\tilde{\mathbf{Y}}) = (\mathbf{I}+\sigma\partial H^*)(\tilde{\mathbf{Y}})$, and thus $\tilde{\mathbf{Y}} = (\mathbf{I}+\sigma\partial H^*)^{-1}(\mathbf{X})$.

In our special case, we find from the definition of H^* in (3.4) that

$$(\mathbf{I}+\sigma\partial H^*)^{-1}(\mathbf{X}) = \operatorname*{argmin}_{\substack{\mathbf{Y}\in\mathbb{R}^{2N\times M}\\ \|\mathbf{Y}\|_\infty\le 1}} \Big(\tfrac{1}{2\sigma}\|\mathbf{X}-\mathbf{Y}\|_F^2\Big),$$

that is, $(\mathbf{I}+\sigma\partial H^*)^{-1}(\mathbf{X})$ is the projection of $\mathbf{X}$ onto the unit ball in $\mathbb{R}^{2N\times M}$ with respect to the Frobenius norm, i.e., $(\mathbf{I}+\sigma\partial H^*)^{-1}(\mathbf{X}) = \tilde{\mathbf{Y}} = \begin{pmatrix}\tilde{\mathbf{Y}}_1\\ \tilde{\mathbf{Y}}_2\end{pmatrix}$ with components

$$\tilde{y}_{\mathbf{k},1} = \tfrac{x_{\mathbf{k},1}}{\max\{1,\sqrt{x_{\mathbf{k},1}^2+x_{\mathbf{k},2}^2}\}}, \qquad \tilde{y}_{\mathbf{k},2} = \tfrac{x_{\mathbf{k},2}}{\max\{1,\sqrt{x_{\mathbf{k},1}^2+x_{\mathbf{k},2}^2}\}}, \quad \mathbf{k}\in\Lambda_{N,M}.$$

To compute $(\mathbf{I}+\tau\partial G)^{-1}(\tilde{\mathbf{A}})$, we recall that the multiplication with an orthonormal matrix leaves the Frobenius norm invariant, such that $\|\tilde{\mathbf{A}}-\mathbf{Z}\|_F^2 = \|\mathbf{F}_N(\tilde{\mathbf{A}}-\mathbf{Z})\mathbf{F}_M\|_F^2 = \|\hat{\tilde{\mathbf{A}}}-\hat{\mathbf{Z}}\|_F^2$. Since $\tilde{\mathbf{A}}$ and $\mathbf{A}$ are both real matrices, we obtain

$$(\mathbf{I}+\tau\partial G)^{-1}(\tilde{\mathbf{A}}) = \operatorname*{argmin}_{\mathbf{Z}\in\mathbb{R}^{N\times M}} \Big(\tfrac{1}{2\tau}\|\tilde{\mathbf{A}}-\mathbf{Z}\|_F^2 + \tfrac{\lambda}{2}\|\mathbf{P}^{(\Lambda)}\circ(\hat{\mathbf{Z}}-\hat{\mathbf{A}})\|_F^2\Big)$$

where

$$\min_{\mathbf{Z}\in\mathbb{R}^{N\times M}}\Big(\tfrac{1}{2\tau}\|\tilde{\mathbf{A}}-\mathbf{Z}\|_F^2+\tfrac{\lambda}{2}\|\mathbf{P}^{(\Lambda)}\circ(\hat{\mathbf{Z}}-\hat{\mathbf{A}})\|_F^2\Big) = \min_{\hat{\mathbf{Z}}\in\mathbb{C}^{N\times M}}\Big(\tfrac{1}{2\tau}\|\hat{\tilde{\mathbf{A}}}-\hat{\mathbf{Z}}\|_F^2+\tfrac{\lambda}{2}\|\mathbf{P}^{(\Lambda)}\circ(\hat{\mathbf{Z}}-\hat{\mathbf{A}})\|_F^2\Big).$$

The solution $\hat{\mathbf{Z}}$ of the minimization problem in Fourier domain satisfies the necessary condition $(\hat{\mathbf{Z}}-\hat{\tilde{\mathbf{A}}}) + \tau\lambda\mathbf{P}^{(\Lambda)}\circ(\hat{\mathbf{Z}}-\hat{\mathbf{A}}) = \mathbf{0}$, i.e.,

$$\hat{\mathbf{Z}} = (\hat{\tilde{\mathbf{A}}} + \tau\lambda\mathbf{P}^{(\Lambda)}\circ\hat{\mathbf{A}})/(\mathbf{E}+\tau\lambda\mathbf{P}^{(\Lambda)}), \tag{3.9}$$

where / denotes the componentwise division and $\mathbf{E}$ is the $(N\times M)$-matrix of ones. Thus, we finally obtain

$$(\mathbf{I}+\tau\partial G)^{-1}(\tilde{\mathbf{A}}) = \mathbf{F}_N^{-1}\hat{\mathbf{Z}}\mathbf{F}_M^{-1} = \mathbf{F}_N^{-1}((\hat{\tilde{\mathbf{A}}} + \tau\lambda\mathbf{P}^{(\Lambda)}\circ\hat{\mathbf{A}})/(\mathbf{E}+\tau\lambda\mathbf{P}^{(\Lambda)}))\mathbf{F}_M^{-1}.$$

The primal-dual algorithm [6] can for our setting be summarized as follows, where here one fixed-point equation is solved in the Fourier domain.

Algorithm 3.1 *(Reconstruction from incomplete Fourier data using TV minimization)*
Input: *incomplete Fourier data* $\mathbf{P}^{(\Lambda)} \circ \hat{\mathbf{A}}$ *of* $\mathbf{A} \in \mathbb{R}^{N\times M}$ *with* $N = 2n$, $M = 2m$,
N *multiple of* 8, $L = 2\ell + 1 < N$,
N_I *number of iterations,*
parameters $\tau > 0$, $\sigma > 0$, $\theta \in [0, 1]$, $\lambda \gg 0$.

Initialization: $\mathbf{A}^{(0)} := \mathbf{F}_N^{-1}(\mathbf{P}^{(\Lambda)} \circ \hat{\mathbf{A}})\mathbf{F}_M$, $\mathbf{X}^{(0)} = \begin{pmatrix} \mathbf{X}_1^{(0)} \\ \mathbf{X}_2^{(0)} \end{pmatrix} := \nabla(\mathbf{A}^{(0)}) = \begin{pmatrix} \mathbf{D}_N\mathbf{A}^{(0)} \\ \mathbf{A}^{(0)}\mathbf{D}_M \end{pmatrix}$.

For $j = 0 : N_I - 1$ *do*

1. *Compute* $\nabla(\mathbf{A}^{(j)}) = \begin{pmatrix} \mathbf{D}_N\mathbf{A}^{(j)} \\ \mathbf{A}^{(j)}\mathbf{D}_M \end{pmatrix}$ *and apply one fixed-point iteration step to solve* (3.7)*, i.e., compute* $\mathbf{X}^{(j+1)} \in \mathbb{C}^{2N\times M}$,
$$\mathbf{X}^{(j+1)} := (\mathbf{X}^{(j)} + (\sigma\nabla(\mathbf{A}^{(j)}))/\max\{1, \|\mathbf{X}^{(j)} + \sigma\nabla(\mathbf{A}^{(j)})\|_\infty\},$$
where / denotes the pointwise division and $\|\mathbf{X}^{(j)} + \nabla(\mathbf{A}^{(j)})\|_\infty$ *is defined according to* (3.2).
2. *Apply one fixed-point iteration step to solve* (3.8).
Write $\mathbf{X}^{(j+1)} = \begin{pmatrix} \mathbf{X}_1^{(j+1)} \\ \mathbf{X}_2^{(j+1)} \end{pmatrix}$ *with* $\mathbf{X}_1^{(j+1)}, \mathbf{X}_2^{(j+1)} \in \mathbb{C}^{N\times M}$ *and compute*
$$\hat{\hat{\mathbf{A}}}^{(j+1)} := \mathbf{F}_N(\mathbf{A}^{(j)} - \nabla^*\mathbf{X}^{(j+1)})\mathbf{F}_M = \mathbf{F}_N(\mathbf{A}^{(j)} - (\mathbf{D}_N\mathbf{X}_1^{(j+1)} + \mathbf{X}_2^{(j+1)}\mathbf{D}_M^T))\mathbf{F}_M.$$
Compute $\hat{\mathbf{A}}^{(j+1)} := (\hat{\hat{\mathbf{A}}}^{(j+1)} + \tau\lambda\mathbf{P}^{(\Lambda)} \circ \hat{\mathbf{A}})/(\mathbf{E} + \tau\lambda\mathbf{P}^{(\Lambda)})$ *with notations as in* (3.9).
Compute $\mathbf{A}^{(j+1)} := \mathbf{F}_N^{-1}\hat{\mathbf{A}}^{(j+1)}\mathbf{F}_M^{-1}$.
3. *Update* $\mathbf{A}^{(j+1)} := \mathbf{A}^{(j+1)} + \theta(\mathbf{A}^{(j+1)} - \mathbf{A}^{(j)})$.

end(for)
Output: $\mathbf{A}^{(TV)} = \mathbf{A}^{(N_I)}$.

As we will see in Section 5, this algorithm usually provides very good reconstruction results which essentially outperform the reconstruction by zero refilling and the interpolation algorithms from Section 2 for reduction rates $r > 2$. Moreover, it is not restricted to the special sampling scheme, which we focussed on in this paper. The convergence of the iteration is ensured for parameters $8\tau\sigma < 1$ as shown in [5, 6]. In our implementation we always use $\theta = 1$ and $\sigma = 0.01 + \frac{1}{8\tau}$ as suggested by Gilles [9].

4 Hybrid method

While Algorithm 3.1 usually provides a very good performance, we want to improve the reconstruction result further by incorporating our knowledge on the structure of the given set of acquired Fourier data. Algorithm 3.1 tends to provide reconstruction results containing staircasing artifacts and with a total variation which is much smaller than that of the original image. For example, for the normalized "cameraman" image, see Figure 4 and Table 1, the total variation, i.e., the sum of all absolute values of $\nabla(\mathbf{A})$, is 9.0603e + 03, while for the resulting image of Algorithm 3.1 for $r = 6$, $L = 43$ in Figure 4 (bottom, middle) the total variation of $\nabla(\tilde{\mathbf{A}}^{(TV)})$ is only 5.5973e + 03. Further, the reconstructions still tend to have an incorrect "distribution" of corresponding index values $\tilde{a}_{k_1,k_2}$ and $\tilde{a}_{k_1-n,k_2}$ at some places in the upper and the lower half of the image. This effect is already strongly reduced compared to the zero refilling reconstruction, but it still exists, see e.g. Figure 6. We recall that this issue is due to the sampling scheme that we have at hand.

The hybrid algorithm that we propose here, is an iterative procedure that locally enlarges the total variation of the image. For this purpose, we start with a smooth approximation $\tilde{\mathbf{A}}^{(0)}$, which is either obtained by Algorithm 3.1 with a regularization parameter λ, which is not too large, or by applying a linear smoothing procedure to the obtained approximation $\tilde{\mathbf{A}}^{(TV)}$ in a first step. Then this initial image $\tilde{\mathbf{A}}^{(0)}$ already provides some knowledge about important local total variations (as edges) of $\mathbf{A}$, but does hardly contain undesirable artifacts caused by badly estimated sums $a_{k_1,k_2} + a_{k_1-n,k_2}$ in the upper and the lower half of the image (as it it happens e.g. in Figure 4 (right) for zero-refilling). The decision, where the total variation of the image approximation should be enlarged, will be taken by comparing the median local total variation (MTV) for every pixel value in the upper half of the image $\tilde{\mathbf{A}}^{(0)}$ with the MTV of the corresponding pixel value in the lower half of the image.

To improve the approximation $\tilde{\mathbf{A}}^{(j)}$ in the j-th iteration step, we consider the difference image $\mathbf{R}^{(j)}$ given by

$$\hat{\mathbf{R}}^{(j)} := \mathbf{P}^{(\Lambda)} \circ (\hat{\mathbf{A}} - \hat{\tilde{\mathbf{A}}}^{(j)}).$$

Then, obviously, $\tilde{\mathbf{A}}^{(j)} + \mathbf{R}^{(j)}$ satisfies $\mathbf{P}^{(\Lambda)} \circ (\hat{\tilde{\mathbf{A}}}^{(j)} + \hat{\mathbf{R}}^{(j)}) = \mathbf{P}^{(\Lambda)} \circ \hat{\mathbf{A}}$. To update the image $\tilde{\mathbf{A}}^{(j)}$, we proceed as follows. If the MTV of $\tilde{a}^{(0)}_{k_1,k_2}$ in the upper half of $\tilde{\mathbf{A}}^{(0)}$ is (significantly) larger than the MTV of $\tilde{a}^{(0)}_{k_1-n,k_2}$ in the lower half, then we add the component $r^{(j)}_{k_1,k_2}$ (or even an amplification $\mu r^{(j)}_{k_1,k_2}$ with $\mu > 1$) of $\mathbf{R}^{(j)}$ to $a^{(j)}_{k_1,k_2}$ while leaving $\tilde{a}^{(j)}_{k_1-n,k_2}$ (almost) untouched, otherwise we add $\mu r^{(j)}_{k_1-n,k_2}$ to $\tilde{a}^{(j)}_{k_1-n,k_2}$ and (almost) do not change $\tilde{a}^{(j)}_{k_1,k_2}$. If the MTV for $\tilde{a}^{(0)}_{k_1,k_2}$ and $\tilde{a}^{(0)}_{k_1-n,k_2}$ is almost of the same size, we add the corresponding (weighted) components of $\mathbf{R}^{(j)}$ at both positions. The rationale behind this procedure is the following. If the local total variation in a neighborhood of a pixel value almost vanishes, then this indicates that the image is locally smooth, i.e., the local total variation should not be enlarged, and the corresponding pixel value is kept, whereas if the local total variation in a neighborhood of a pixel value is large, then this indicates an important feature and the local total variation should be enlarged.

We will show that this iteration leads to an image reconstruction $\tilde{\mathbf{A}}$ that satisfies the Fourier data constraints (1.3).

To compute the MTV, we apply the following formulas. First we compute the local total variations of $\tilde{\mathbf{A}}^{(0)}$ at all pixels (k_1, k_2),

$$\mathrm{TV}(k_1, k_2) := \sum_{j_2=-1}^{1} |\tilde{a}^{(0)}_{k_1,k_2} - \tilde{a}^{(0)}_{k_1,k_2-j_2}| + \sum_{j_1=-1}^{2} \sum_{j_2=-1}^{1} |\tilde{a}^{(0)}_{k_1-j_1+1,k_2-j_2} - \tilde{a}^{(0)}_{k_1-j_1,k_2-j_2}|, \quad (4.1)$$

where for boundary pixels only existing neighbor values are taken. Then we consider the median of the local TV values in a fixed window $[-\gamma_1, \gamma_1] \times [-\gamma_2, \gamma_2]$ around (k_1, k_2),

$$\mathrm{MTV}(k_1, k_2) := \mathrm{median}((\mathrm{TV}(k_1 + j_1, k_2 + j_2)^{\gamma_1,\gamma_2}_{j_1=-\gamma_1, j_2=-\gamma_2}) \quad (4.2)$$

for $k_1 = -n \ldots, n-1$, $k_2 = -m, \ldots, m-1$, where for boundary pixels only the remaining values of the window $[-\gamma_1, \gamma_1] \times [-\gamma_2, \gamma_2]$ are involved. At each iteration step, we can either always take the same local TV and MTV values obtained from the initial image $\tilde{\mathbf{A}}^{(0)}$, or update these values using $\tilde{\mathbf{A}}^{(j)}$. The image update $\tilde{\mathbf{A}}^{(j+1)}$ is then derived by

$$\tilde{\mathbf{A}}^{(j+1)} = \tilde{\mathbf{A}}^{(j)} + \mu(\mathbf{W} \circ \mathbf{R}^{(j)})$$

with $\mu \in [1, 2)$ and a weight matrix $\mathbf{W} = (\mathsf{w}_{k_1,k_2})_{k_1=-n,k_2=-m}^{n-1,m-1} \in \mathbb{R}^{N \times M}$ which is determined according to the MTV values at every pixel,

$$\mathsf{w}_{k_1,k_2} := \begin{cases} 1-\epsilon & |MTV(k_1,k_2)| > 1.5|MTV(k_1 \pm n, k_2)|, \\ \epsilon & |MTV(k_1 \pm n, k_2)| > 1.5|MTV(k_1,k_2)|, \\ \frac{MTV(k_1,k_2)}{MTV(k_1,k_2)+MTV(k_1 \pm n,k_2)} & \text{otherwise}, \end{cases} \tag{4.3}$$

where $\pm$ means that we take $+$ for $k_1 < 0$ and $-$ for $k_1 \geq 0$. The parameter $\epsilon > 0$ is taken to be small, in the numerical experiments we have used $\epsilon = 0.05$ or $\epsilon = 0.1$. This procedure is repeated until the remainder $\mathbf{R}^{(j)}$ is close to the zero matrix. The algorithm is summarized as follows.

Algorithm 4.1 *(Image reconstruction improvement from incomplete Fourier data)*
Input: *incomplete Fourier data* $\mathbf{P}^{(\Lambda)} \circ \hat{\mathbf{A}}$ *of* $\mathbf{A} \in \mathbb{R}^{N \times M}$ *with* $N = 2n$, $M = 2m$,
$\tilde{\mathbf{A}}^{(TV)}$ *reconstructed image of Algorithm* 3.1.
N *multiple of* 8, $L = 2\ell + 1 < N$,
N_I *number of iterations for reconstruction,*
N_s *number of iterations for linear smoothing,*
$\mu \in [1, 2)$ *parameter for frequency reconstruction,*
(γ_1, γ_2) *local window size for local TV computation,*
$\epsilon < 0$ *(e.g.* $0.05 \leq \epsilon \leq 0.1$*).*

1. *(Optional) Apply a smoothing filter to every column of* $\tilde{\mathbf{A}}^{(TV)} = (\tilde{a}_{k_1,k_2}^{(TV,0)})_{k_1=-n,k_2=-m}^{n-1,m-1}$.
   For $s = 0 : N_s - 1$
   For $k_2 = -m : m - 1$

$$\tilde{a}_{k_1,k_2}^{(TV,s+1)} := \begin{cases} \frac{1}{4}(\tilde{a}_{k_1-1,k_2}^{(TV,s)} + 2\tilde{a}_{k_1,k_2}^{(TV,s)} + \tilde{a}_{k_1+1,k_2}^{(TV,s)}) & -n+1 \leq k_1 \leq n-2, \\ \frac{1}{4}(3\tilde{a}_{k_1,k_2}^{(TV,s)} + \tilde{a}_{k_1+1,k_2}^{(TV,s)}) & k_1 = -n, \\ \frac{1}{4}(\tilde{a}_{k_1-1,k_2}^{(TV,s)} + 3\tilde{a}_{k_1,k_2}^{(TV,s)}) & k_1 = n-1. \end{cases}$$

   Set $\tilde{\mathbf{A}}^{(0)} := \tilde{\mathbf{A}}^{(TV,N_s)} = (\tilde{a}_{k_1,k_2}^{(0)})_{k_1=-n,k_2=-m}^{n-1,m-1}$.

2. *Compute the local total variation* $TV(k_1, k_2)$ *of* $\tilde{\mathbf{A}}^{(0)} = (\tilde{a}_{k_1,k_2}^{(0)})_{k_1=-n,k_2=-m}^{n-1,m-1}$ *according to* (4.1) *for* $k_1 = -n, \ldots, n-1$, $k_2 = -m, \ldots, m-1$.
   Compute the median local total variation $MTV(k_1, k_2)$ *in* (4.2) *for* $k_1 = -n \ldots, n-1$, $k_2 = -m, \ldots, m-1$.

3. *Compute the matrix of weights* $\mathbf{W} := (\mathsf{w}_{k_1,k_2})_{k_1=-n,k_2=-m}^{n-1,m-1}$ *as given in* (4.3).

4. *For* $j = 0 : N_I - 1$ *do*
   (a) *Compute* $\hat{\tilde{\mathbf{A}}}^{(j)} := \mathbf{F}_N \tilde{\mathbf{A}}^{(j)} \mathbf{F}_M$ *and* $\mathbf{R}^{(j)} := \mathbf{F}_N^{-1}(\mathbf{P}^{(\Lambda)} \circ (\hat{\mathbf{A}} - \hat{\tilde{\mathbf{A}}}^{(j)}))\mathbf{F}_M^{-1}$.
   (b) *Compute the update*

$$\tilde{\mathbf{A}}^{(j+1)} := \tilde{\mathbf{A}}^{(j)} + \mu \, \mathbf{W} \circ \mathbf{R}^{(j)}.$$

   end(do)

Output: *Image reconstruction* $\tilde{\mathbf{A}}^{(N_I)}$.

Instead of fixing the number of iterations N_I in Step 4 of Algorithm 4.1, we can also apply a stopping criteria based on the Frobenius norm of the remainder $\mathbf{R}^{(j)}$. Next, we show that Algorithm 4.1 always converges to an image satisfying the constraint $\mathbf{P}^{(\Lambda)} \circ \hat{\mathbf{A}} = \lim\limits_{N_I \to \infty} (\mathbf{P}^{(\Lambda)} \circ \hat{\tilde{\mathbf{A}}}^{(N_I)})$.

Theorem 4.2 *For given Fourier data* $\mathbf{P}^{(\Lambda)} \circ \hat{\mathbf{A}}$ *with* Λ *in* (1.1)*, Algorithm* 4.1 *converges for* $\mu \in [1, 2)$ *to an image* $\tilde{\mathbf{A}} = \lim\limits_{N_I \to \infty} \tilde{\mathbf{A}}^{(N_I)}$ *satisfying* $\mathbf{P}^{(\Lambda)} \circ \hat{\mathbf{A}} = \mathbf{P}^{(\Lambda)} \circ \hat{\tilde{\mathbf{A}}}$.

Proof: It is sufficient to show that $\lim\limits_{j \to \infty} \mathbf{R}^{(j)} = \mathbf{0}$ for $\mathbf{R}^{(j)} = \mathbf{F}_N^{-1}(\mathbf{P}^{(\Lambda)} \circ (\hat{\mathbf{A}} - \hat{\tilde{\mathbf{A}}}^{(j)}))\mathbf{F}_M^{-1}$. Step 4 of Algorithm 4.1 yields with $\hat{\mathbf{R}}^{(0)} = \mathbf{F}_N \mathbf{R}^{(0)} \mathbf{F}_M = \mathbf{P}^{(\Lambda)} \circ (\hat{\mathbf{A}} - \hat{\tilde{\mathbf{A}}}^{(0)})$ the recursion formula

$$\begin{aligned}\hat{\mathbf{R}}^{(j+1)} &= \mathbf{P}^{(\Lambda)} \circ (\hat{\mathbf{A}} - \hat{\tilde{\mathbf{A}}}^{(j+1)}) = \mathbf{P}^{(\Lambda)} \circ (\hat{\mathbf{A}} - (\hat{\tilde{\mathbf{A}}}^{(j)} + \mu\, \mathbf{F}_N(\mathbf{W} \circ \mathbf{R}^{(j)})\mathbf{F}_M)) \\ &= \hat{\mathbf{R}}^{(j)} - \mu \mathbf{P}^{(\Lambda)} \circ (\mathbf{F}_N(\mathbf{W} \circ \mathbf{R}^{(j)})\mathbf{F}_M) = \mathbf{P}^{(\Lambda)} \circ (\hat{\mathbf{R}}^{(j)} - \mu(\mathbf{F}_N(\mathbf{W} \circ \mathbf{R}^{(j)})\mathbf{F}_M)) \\ &= \mathbf{P}^{(\Lambda)} \circ (\mathbf{F}_N(\mathbf{R}^{(j)} - \mu(\mathbf{W} \circ \mathbf{R}^{(j)}))\mathbf{F}_M),\end{aligned}$$

since $\hat{\mathbf{R}}^{(j)}$ has by definition vanishing components for all $\boldsymbol{\nu} = (\nu_1, \nu_2) \notin \Lambda$. Taking the inverse Fourier transform and applying vectorization on both sides of the equation leads to

$$\mathrm{vec}(\mathbf{R}^{(j+1)}) = (\mathbf{F}_M \otimes \mathbf{F}_N)^{-1} \mathrm{diag}(\mathrm{vec}(\mathbf{P}^{(\Lambda)}))(\mathbf{F}_M \otimes \mathbf{F}_N)(\mathbf{I}_{MN} - \mu \mathrm{diag}(\mathrm{vec}(\mathbf{W})))\mathrm{vec}(\mathbf{R}^{(j)}), \tag{4.4}$$

where we have used that $\mathrm{vec}(\mathbf{F}_N \mathbf{R}^{(j)} \mathbf{F}_M) = (\mathbf{F}_M \otimes \mathbf{F}_N)\mathrm{vec}(\mathbf{R}^{(j)})$, see e.g. [21], Section 3.4. We observe that all matrix factors in (4.4) have a spectral norm smaller than or equal to one. In particular, $(\mathbf{F}_M \otimes \mathbf{F}_N)$ is orthonormal, $\mathrm{diag}(\mathrm{vec}(\mathbf{P}^{(\Lambda)}))$ only contains zeros or ones in the diagonal, and $(\mathbf{I}_{MN} - \mu\, \mathrm{diag}(\mathrm{vec}(\mathbf{W})))$ contains diagonal entries $1 - \mu \mathsf{w}_{k_1,k_2} \in (-1 + 2\epsilon, 1 - \epsilon]$, since $\mu \in [1, 2)$, $\mathsf{w}_{k_1,k_2} \in [\epsilon, 1 - \epsilon]$. Thus, the spectral radius of $(\mathbf{I}_{MN} - \mu\, \mathrm{diag}(\mathrm{vec}(\mathbf{W})))$ is at most $1 - \epsilon$, and we can directly conclude that

$$\|\mathrm{vec}(\mathbf{R}^{(j+1)})\|_2 \leq (1 - \epsilon)\|\mathrm{vec}(\mathbf{R}^{(j)})\|_2,$$

such that convergence is ensured for $j \to \infty$. ■

5 Numerical Results

In this section we compare the described algorithms for reconstruction from structured incomplete Fourier data with emphasis to the sampling pattern given in (1.1). We particularly consider different images of size 512×512 and compare the PSNR (peak signal to noise ratio) for the reconstruction methods zero refilling in Section 2.2, local interpolation in Section 2.5, TV functional minimization in Section 3, the hybrid method in Section 4, and the low-pass reconstruction, obtained if for a reduction rate r, we simply take all middle rows with indices $-\lfloor \frac{N}{2r} \rfloor, \ldots, \lfloor \frac{N}{2r} \rfloor$. All used images are "Standard" test images and have been taken from the open source platform `https://www.imageprocessingplace.com/root_` `files_V3/image_databases.htm`. The MATLAB software to reproduce the results in this section can be found at `https://na.math.uni-goettingen.de` under `software`.

We will study reduction rates $r = 2, 4, 6, 8$, taking in the corresponding experiments 256, 128, 85 or 64 rows according to the scheme fixed in (1.1). Recall that for the considered real images this corresponds to almost double reduction rates upt to 16, since we have $\hat{a}_{\boldsymbol{\nu}} = \overline{\hat{a}}_{-\boldsymbol{\nu}}$. For the low-pass area we consider different sizes, in particular $L = 43$ (for all r), $L = 63$ (for $r = 2, 4, 6$), $L = 83$ (for $r = 2, 4$), $L = 103$ for $r = 4$, and $L = 163$ for $r = 2$. For all three reconstructed images, the blue colored PSNR values in Tables 1,2,3 indicate the best reconstruction result for the considered reduction rate.

The reconstruction results for the 512×512 image "cameraman" are given in Table 1, see also Figure 4 for the special case of reduction rate $r = 6$, where 85 rows of the 512 rows of $\hat{\mathbf{A}}$ are acquired. The interpolation algorithm uses a local window of size 11×11 for the interpolation weights. For Algorithm 3.1 (TV-minimization) we have always used the parameters $N_I = 250$, $\tau = 0.03$, $\theta = 1.0$, $\sigma = 0.01 + 1/(8\tau)$ and $\lambda = 100$. For the Hybrid Algorithm 4.1 we have taken the result of Algorithm 3.1 as the initial image, $N_I = 10$, $N_s = 3$, $\mu = 1.6$, $\epsilon = 0.05$, and window size $\gamma_1 = \gamma_3 = 3$.

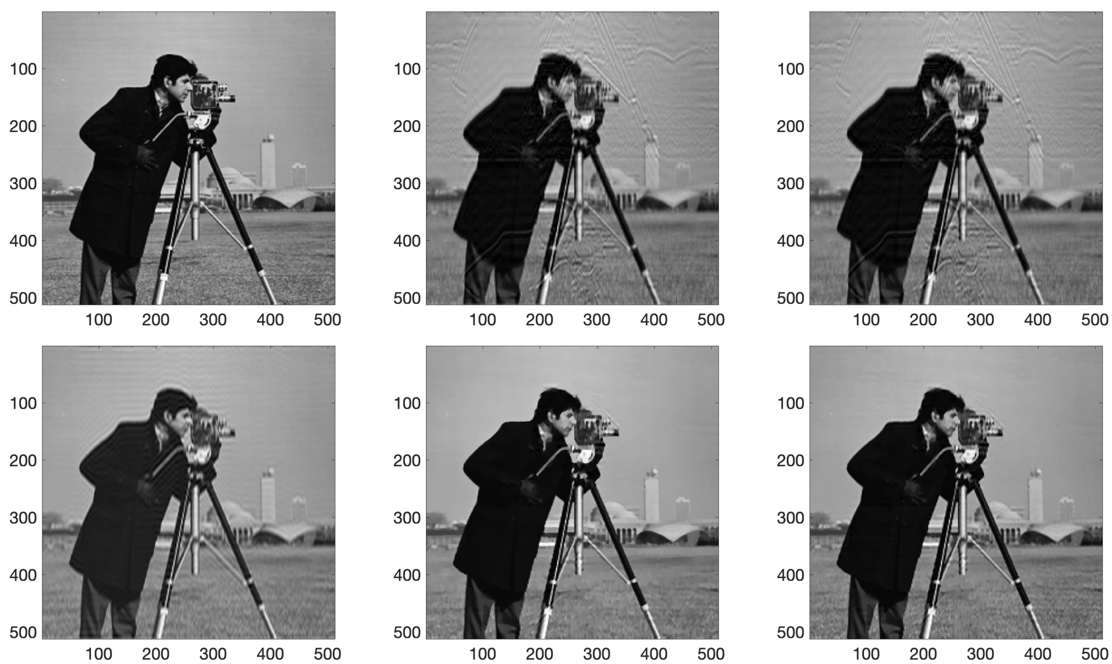

Figure 4: Image reconstructions for reduction rate 6. Top: Left: "cameraman" original image 512×512; Middle: reconstruction by zero refilling for $L = 43$ with PSNR 27.6986; Right: reconstruction by interpolation of Fourier data (GRAPPA) for $L = 43$ with PSNR 27.7064; Bottom: Left: low-pass reconstruction from $\lfloor \frac{N}{6} \rfloor = 85$ rows with PSNR 29.0115; Middle: reconstruction by TV minimization for $L = 43$ with PSNR 31.1364; Right: reconstruction by hybrid method for $L = 43$ with PSNR 32.1167

The reconstruction results for the 512×512 image "boat" are given in Table 2. In Figure 5 we present the obtained reconstructions for the special case of reduction rate $r = 4$, where 128 rows of the 512 rows of $\hat{\mathbf{A}}$ are acquired, with a low-pass area containing $L = 103$ centered rows. For Algorithm 3.1 (TV-minimization) we applied the parameters $N_I = 250$, $\tau = 0.03$, $\theta = 1.0$, $\sigma = 0.01 + 1/(8\tau)$ and $\lambda = 100$ for $r = 4, 6, 8$. For reduction rate $r = 2$, we used $\lambda = 100$ for $L = 43$, 63, 83, $\lambda = 200$ for $L = 103$, and $\lambda = 500$ for

Table 1: Comparison of the reconstruction performance for incomplete Fourier data for the 512×512 "cameraman" image (PSNR values)

reduction rate	low-pass width	zero refilling	low pass	interpolation	TV-minimization	hybrid
$r = 2$	$L = 43$	28.4611	**42.1126**	28.6108	34.2899	35.6529
$r = 2$	$L = 63$	30.4380	**42.1126**	30.4282	35.8917	37.5627
$r = 2$	$L = 83$	31.9667	**42.1126**	31.9652	36.9517	39.0341
$r = 2$	$L = 103$	33.6619	**42.1126**	33.6409	37.8479	40.4848
$r = 2$	$L = 163$	38.4152	42.1126	38.4017	39.5615	**43.9808**
$r = 2$	$L = 183$	39.7616	42.1126	39.7681	39.6578	**44.5272**
$r = 4$	$L = 43$	28.2920	32.5435	28.4313	33.4018	**34.8641**
$r = 4$	$L = 63$	30.0766	32.5435	30.0655	34.1703	**35.8480**
$r = 4$	$L = 83$	31.2739	32.5435	31.2704	34.1724	**35.9945**
$r = 4$	$L = 103$	32.2709	32.5435	32.2589	33.7976	**35.5006**
$r = 6$	$L = 43$	27.6986	29.0115	27.8012	31.1364	**32.1167**
$r = 6$	$L = 63$	28.8521	29.0115	28.8466	30.7164	**31.6398**
$r = 8$	$L = 35$	26.3523	27.2604	26.3809	29.2534	**29.8214**
$r = 8$	$L = 43$	26.8194	27.2604	26.8797	29.0807	**29.6174**

$L = 163, 183, 223$. For the Hybrid Algorithm 4.1 we took the result of Algorithm 3.1 as the initial image, $N_I \leq 10$, $\mu = 1.6$, $\epsilon = 0.1$, window size $\gamma_1 = \gamma_2 = 3$. Further, we applied two smoothing steps ($N_s = 2$) for $r = 4, 6, 8$ and $r = 2$ with $L \leq 83$ and only one smoothing step for $r = 2$ and $L \geq 103$. The interpolation algorithm uses a local window of size 11×11 to compute the interpolation weights form the low-pass area.

Table 2: Comparison of the reconstruction performance for incomplete Fourier data for the 512×512 "boat" image (PSNR values)

reduction rate	low-pass width	zero refilling	low pass	interpolation	TV-minimization	hybrid
$r = 2$	$L = 43$	27.5472	**38.2040**	27.5607	30.4695	30.9669
$r = 2$	$L = 63$	29.2590	**38.2040**	29.2600	31.7578	32.4685
$r = 2$	$L = 83$	30.6754	**38.2040**	30.6383	32.8004	33.7145
$r = 2$	$L = 103$	32.1627	**38.2040**	32.1603	34.2960	34.9480
$r = 2$	$L = 163$	35.5347	**38.2040**	35.5281	36.6132	37.6673
$r = 2$	$L = 183$	36.4173	38.2040	36.4159	36.9317	**38.2358**
$r = 2$	$L = 223$	37.8877	38.2040	37.8881	37.0482	**38.8041**
$r = 4$	$L = 43$	27.2689	**30.6800**	27.2808	29.7853	30.4302
$r = 4$	$L = 63$	28.7329	30.6800	28.7340	30.5864	**31.4227**
$r = 4$	$L = 83$	29.7577	30.6800	29.7333	30.8849	**31.8436**
$r = 4$	$L = 103$	30.5436	30.6800	30.5414	30.8942	**31.9183**
$r = 6$	$L = 43$	26.6263	27.7886	26.6326	28.5838	**29.1021**
$r = 6$	$L = 63$	27.5990	27.7886	27.6004	28.6371	**29.1912**
$r = 8$	$L = 35$	25.3020	26.1116	25.2796	27.0459	**27.4014**
$r = 8$	$L = 43$	25.8638	26.1116	25.8638	27.2016	**27.5753**

For the last example, the best results for different reduction rates in presented in Figure 7.

Next, we consider the MRI "phantom" image of size 512×512, see Table 3 and Figure 6. Because of the special cartoon-like structure of this image, the Hybrid Algorithm 4.1 does not add much improvement to the results achieved by the TV minimization. In contrast to the other images, for higher reduction rates we obtain better recovery results when taking a low-pass area with smaller width L, since it is more important here to catch the higher frequencies. For Algorithm 3.1 (TV-minimization) we applied the parameters $N_I = 250$, $\tau = 0.03$, $\theta = 1.0$, $\sigma = 0.01 + 1/(8\tau)$ and $\lambda = 500$. For the Hybrid Algorithm 4.1 we took the result of Algorithm 3.1 as the initial image, applied one smoothing step

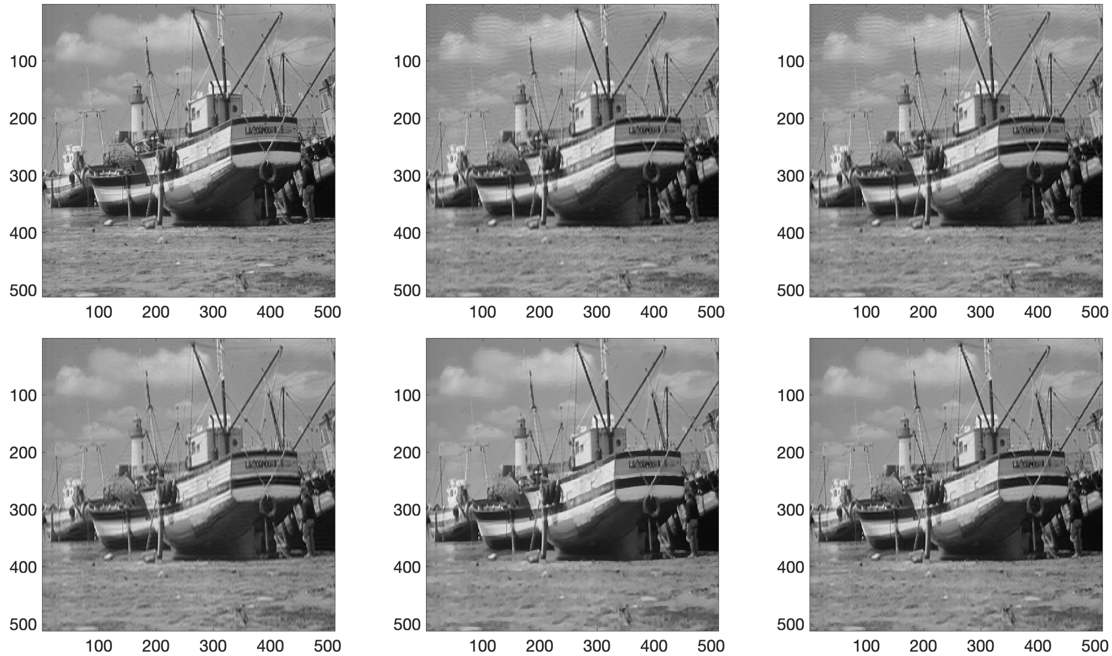

Figure 5: Image reconstructions for reduction rate 4. Top: Left: ”boat” original image 512×512; Middle: reconstruction by zero refilling with $L = 103$ and PSNR 30.5436; Right: reconstruction by interpolation of Fourier data (GRAPPA) with $L = 103$ and PSNR 30.5419; Bottom: Left: low-pass reconstruction from $\lfloor \frac{N}{4} \rfloor = 128$ rows with PSNR 30.8040; Middle: reconstruction by TV minimization with $L = 103$ and PSNR 30.8942; Right: reconstruction by hybrid method with $L = 103$ and PSNR 31.9183

Table 3: Comparison of the reconstruction performance for incomplete Fourier data for the 512×512 “phantom” image (PSNR values)

reduction rate	low-pass width	zero refilling	low pass	interpolation	TV-minimization	hybrid
$r = 2$	$L = 43$	28.0710	36.5454	30.5464	41.3545	**41.7740**
$r = 2$	$L = 63$	29.8508	36.5454	32.6006	42.6828	**43.2157**
$r = 2$	$L = 83$	31.3967	36.5454	34.0137	43.1131	**43.6607**
$r = 2$	$L = 103$	32.9290	36.5454	35.2493	42.9847	**43.5047**
$r = 2$	$L = 163$	35.8249	36.5454	37.1173	41.9584	**42.3462**
$r = 4$	$L = 35$	26.5838	31.5192	28.8051	37.1276	**37.2101**
$r = 4$	$L = 43$	27.6676	31.5192	29.6379	37.2433	**37.3264**
$r = 4$	$L = 63$	29.1792	31.5192	31.0389	37.3916	**37.4674**
$r = 4$	$L = 83$	30.3271	31.5192	31.7063	37.1588	**37.2312**
$r = 6$	$L = 27$	25.5429	28.2569	27.4372	35.2243	**35.2759**
$r = 6$	$L = 35$	26.2189	28.2569	28.0077	35.1240	**35.1703**
$r = 6$	$L = 43$	27.1459	28.2569	28.5582	34.9036	**34.9483**
$r = 6$	$L = 63$	28.0999	28.2569	28.9733	33.2123	**33.2621**
$r = 8$	$L = 19$	24.0342	26.4199	25.2564	32.2327	**32.2591**
$r = 8$	$L = 27$	25.1295	26.4199	26.5647	31.9117	**31.9433**
$r = 8$	$L = 35$	25.6499	26.4199	26.8477	31.0930	**31.2566**
$r = 8$	$L = 43$	26.2553	26.4199	26.9402	30.2271	**30.4698**

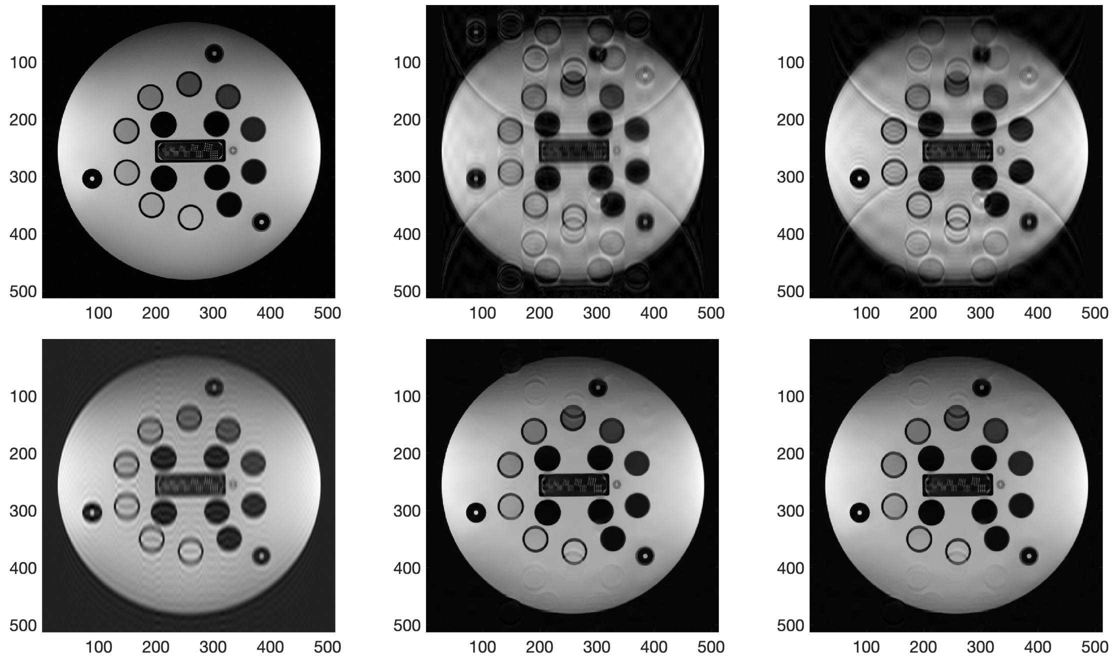

Figure 6: Image reconstructions for reduction rate 8 and $L = 19$. Top: Left: “phantom” original image 512×512; Middle: reconstruction by zero refilling with PSNR 24.0342; Right: reconstruction by interpolation of Fourier data (GRAPPA) with PSNR 25.2564 Bottom: Left: low-pass reconstruction from $\lfloor \frac{N}{8} \rfloor = 64$ rows with PSNR 26.4199; Middle: reconstruction by TV minimization with PSNR 32.1632; Right: reconstruction by hybrid method with PSNR 32.1929

$N_s = 1$ for $r = 8$, $L = 35$, 43, and $N_s = 0$ otherwise, $N_I \leq 15$, $\mu = 1.6$, $\epsilon = 0.1$, window size $\gamma_1 = \gamma_3 = 3$. The interpolation algorithm uses a local window of size 11×11 to compute the interpolation weights form the low-pass area. For interpolation we employed the implementation by M. Lustig in the ESPIRiT toolbox for the special case of only one coil, which for this image provided better results than our implementation (in contrast to the other two images).

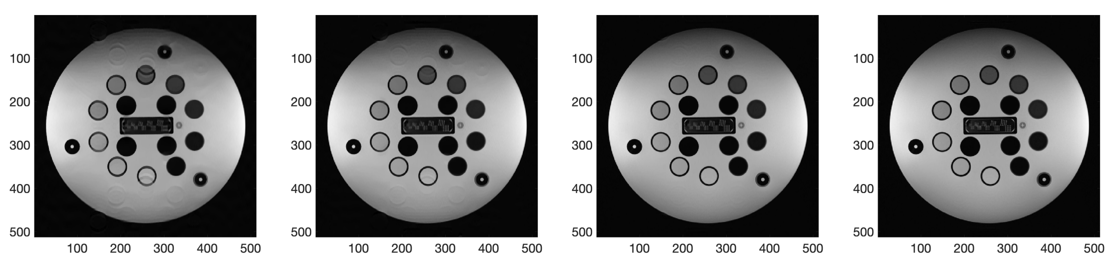

Figure 7: Best image reconstructions using the proposed hybrid method for the “phantom” image for different reduction rates. From left to right: first: $r = 8$, $L = 17$; second: $r = 6$, $L = 27$; third: $r = 4$, $L = 63$; fourth: $r = 2$, $L = 83$

Finally, we compare the image reconstruction results using Algorithm 3.1 for the ”cameraman” image for different sampling patterns. We compare our sampling set Λ in (1.1) with sampling sets Λ_3 and Λ_4, where beside the lowpass set $\Lambda_{L,M}$, in Λ_3 every third row, and in Λ_4 each fourth row of $\hat{\mathbf{A}}$ is acquired until the number of $\lfloor \frac{N}{r} \rfloor$ is reached, see Figure 8. Algorithm 3.1 is applied here with $N_I = 250$, $\tau = 0.03$, $\theta = 1.0$, $\sigma = 0.01 + 1/(8\tau)$

and $\lambda = 500$. The results of this comparison, presented in Table 4, show that these other sampling strategies usually do not lead to better reconstruction results, compared to the set Λ in (1.1).

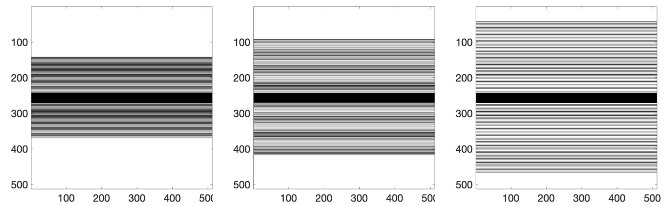

Figure 8: Masks for acquired Fourier data for $r = 4$ and $L = 27$ for Λ (every second line), Λ_3 (every third line) and Λ_4 (every fourth line) beside the low-pass set

Table 4: Comparison of the reconstruction performance for incomplete Fourier data for the 512×512 "cameraman" image for different sampling sets (PSNR values)

reduction rate	low-pass width	sampling set Λ	sampling set Λ_3	sampling set Λ_4
$r = 4$	$L = 43$	**33.6802**	27.3641	30.0970
$r = 4$	$L = 63$	**34.6699**	29.3119	32.0558
$r = 4$	$L = 83$	**34.6659**	33.4319	33.3220
$r = 6$	$L = 35$	**31.0799**	29.5245	28.8486
$r = 6$	$L = 43$	**31.2923**	26.8227	29.9065
$r = 6$	$L = 63$	30.8950	28.8150	**31.1178**
$r = 8$	$L = 27$	**29.2082**	24.6907	27.6181
$r = 8$	$L = 35$	**29.3146**	28.8143	28.5050
$r = 8$	$L = 43$	29.1544	26.7357	**29.1909**

6 Conclusion

Our study of image recovery from structured 2D DFT data and the numerical experiments provide several interesting insights.

The reconstruction results achieved with the presented methods strongly depend on the considered images. Clearly, images containing many small details, which correspond to more information in high Fourier frequencies can be reconstructed only with smaller accuracy. Our proposed Hybrid Algorithm 4.1 always leads to essentially better reconstruction results than a low-pass reconstruction.

Using the sampling pattern (1.1) the width L of the low-pass area plays an important role for the reconstruction performance, where the best choice of L depends on the specific image. Cartoon like images (such as the "phantom" image) can be better reconstructed taking a low-pass area with smaller width L, while the further band- and high-pass information provided by the rows of Fourier data outside the low-pass area is very important. For the "cameraman" image, the Hybrid Algorithm 4.1 essentially improves the PSNR result of the TV minimization, while for the "phantom" image only slight improvements are obtained.

Taking Algorithm 4.1, which can be also seen as a post-processing method when taking the results of Algorithm 3.1 as input, we can achieve very good reconstruction performance while using a rather low number of iteration steps for TV minimization.

The new insights about suitable sampling patterns achieved here will be exploited to improve current approaches for image recovery in parallel MRI, where a full set of undersampled k-space data of coil images is available to reconstruct the desired magnetization image.

Acknowledgements

Gerlind Plonka acknowledges funding from the European Union's Horizon 2020 Research and Innovation Staff Exchange program under the MSCA grant agreement No. 101008231 (EXPOWER) and from German Research Foundation in the framework of the CRC 1456. Anahita Riahi acknowledges support by the German Research Foundation in the framework of the RTG 2088.

Declarations

Data Availability. All used images are "Standard" test images and have been taken from the open source platform `https://www.imageprocessingplace.com/root_files_V3/image_databases.htm`. The MATLAB software to reproduce the numerical results in this paper can be found at `https://na.math.uni-goettingen.de` under `software`.

Conflict of Interest. The authors declare no competing interests.

References

[1] R. Archibald, A. Gelb, and R. Platte, *Image reconstruction from undersampled Fourier data using the polynomial annihilation transform*, J. Sci. Comput., 67 (2016), pp. 432–452.

[2] K. T. Block, M. Uecker, and J. Frahm, *Undersampled radial MRI with multiple coils. iterative image reconstruction using a total variation constraint*, Magnetic Resonance in Medicine, 57 (2007), pp. 1086–1098.

[3] J. Borwein and A. Lewis, *Convex Analysis and Nonlinear Optimization: Theory and Examples*, Springer New York, 2nd ed., 2006.

[4] E. Candes, J. Romberg, and T. Tao, *Robust uncertainty principles: exact signal reconstruction from highly incomplete frequency information*, IEEE Transactions on Information Theory, 52 (2006), pp. 489–509.

[5] A. Chambolle, *An algorithm for total variation minimization and applications*, J. Math. Imaging Vis., 20 (2004), pp. 89–97.

[6] A. Chambolle and T. Pock, *A first-order primal-dual algorithm for convex problems with applications to imaging*, J. Math. Imaging Vis., 40 (2010), pp. 120–145.

[7] ——, *An introduction to continuous optimization for imaging*, Acta Numerica, 25 (2016), pp. 161–319.

[8] L. Feng, R. Grimm, K. Block, H. Chandarana, S. Kim, J. Xu, L. Axel, D. Sodickson, and R. Otazo, *Golden-angle radial sparse parallel MRI: combination of compressed sensing, parallel imaging, and golden-angle radial sampling for fast and flexible dynamic volumetric MRI*, Magn. Reson. Med., 72 (2014), pp. 707–717.

[9] J. Gilles, *PrimalDual-Matlab, https://github.com/jegilles/PrimalDual-Matlab*, 2024.

[10] M. Griswold, P. M. Jakob, R. Heidemann, M. Nittka, V. Jellus, J. Wang, B. Kiefer, and A. Haase, *Generalized autocalibrating partially parallel acquisitions (GRAPPA)*, Magn. Reson. Med., 47 (2002), pp. 1202–1210.

[11] C. M. Hyun, H. P. Kim, S. M. Lee, S. Lee, and J. K. Seo, *Deep learning for undersampled MRI reconstruction*, Physics in Medicine & Biology, 63 (2018), p. 135007.

[12] P. Jakob, M. Griswold, R. Edelman, and D. Sodickson, *AUTO-SMASH: a self-calibrating technique for SMASH imaging*, Magn. Reson. Med., 7 (1998), pp. 42–54.

[13] J. Karp, G. Muehllehner, and R. M. Lewitt, *Constrained Fourier space method for compensation of missing data in emission computed tomography*, IEEE Trans. Med. Imaging, 7 (1988), pp. 21–25.

[14] S. L. Keeling, C. Clason, M. Hintermüller, F. Knoll, A. Laurain, and G. von Winckel, *An image space approach to Cartesian based parallel MR imaging with total variation regularization*, Med. Image Anal., 16 (2012), pp. 189–200.

[15] F. Knoll, K. Bredies, T. Pock, and R. Stollberger, *Second order total generalized variation (TGV) for MRI*, Magnetic Resonance in Medicine, 65 (2011), pp. 480–491.

[16] F. Knoll, K. Hammernik, C. Zhang, S. Moeller, T. Pock, D. Sodickson, and M. Akçakaya, *Deep-learning methods for parallel magnetic resonance imaging reconstruction: A survey of the current approaches, trends, and issues*, IEEE Signal Process. Mag., 37 (2020), pp. 128–140.

[17] F. Krahmer and H. Rauhut, *Structured random measurements in signal processing*, GAMM-Mitt., 39 (2014), pp. 217–238.

[18] M. Lustig, D. Donoho, and J. M. Pauly, *Sparse mri: The application of compressed sensing for rapid MR imaging*, Magnetic Resonance in Medicine, 58 (2007), pp. 1182–1195.

[19] M. Lustig and J. Pauly, *SPIRIT: Iterative self-consistent parallel imaging reconstruction from arbitrary k-space*, Mag. Reson. Med., 64 (2010), pp. 457–471.

[20] M. J. Muckley, D. C. Noll, and J. A. Fessler, *Fast parallel MR image reconstruction via B1-based, adaptive restart, iterative soft thresholding algorithms (BARISTA)*, IEEE Trans. Med. Imaging, 34 (2015), pp. 578–588.

[21] G. Plonka, D. Potts, G. Steidl, and M. Tasche, *Numerical Fourier Analysis*, Birkhäuser, Cham, 2nd ed., 2023.

[22] G. Plonka and Y. Riebe, *MOCCA: A fast algorithm for parallel MRI reconstruction using model based coil calibration*, preprint, (2024), p. 32 pages.

[23] M. I. Sezan and H. Stark, *Tomographic image reconstruction from incomplete view data by convex projections and direct Fourier inversion*, IEEE Trans. Med. Imaging, 3 (1984), pp. 91–98.

[24] M. Uecker, P. Lai, M. J. Murphy, P. Virtue, M. Elad, J. Pauly, S. Vasanawala, and M. Lustig, *ESPIRiT—an eigenvalue approach to autocalibrating parallel MRI: Where SENSE meets GRAPPA*, Magn. Reson. Med., 71 (2014), pp. 990–1001.

[25] T. Wu, L. Shen, and Y. Xu, *Fixed-point proximity algorithms solving an incomplete Fourier transform model for seismic wavefield modeling*, Journal of Computational and Applied Mathematics, 385 (2021), p. 113208.

[26] Y. Xiao, J. Glaubitz, A. Gelb, and G. Song, *Sequential image recovery from noisy and under-sampled Fourier data*, J. Sci. Comput., 91 (2022), p. 79.

[27] J. Yang, Y. Zhang, and W. Yin, *A fast alternating direction method for TVL1-L2 signal reconstruction from partial Fourier data*, IEEE Journal of Selected Topics in Signal Processing, 4 (2010), pp. 288–297.

[28] M. Zhang, M. Zhang, F. Zhang, A. Chaddad, and A. Evans, *Robust brain MR image compressive sensing via re-weighted total variation and sparse regression*, Magnetic Resonance Imaging, 85 (2022), pp. 271–286.